A rabbit sized phantom for validation of quantitative imaging of magnetic nanoparticle distributions

M. Liebl[1,2], U. Steinhoff[1], F. Wiekhorst[1], D. Baumgarten[2], D. Gutkelch[1], L. Trahms[1], J. Haueisen[2]
[1]Physikalisch-Technische Bundesanstalt, Berlin, Germany
[2]Technical University Ilmenau, Institute of Biomedical Engineering and Informatics, Ilmenau, Germany

Introduction

For novel biomedical applications of magnetic nanoparticles (MNP) like magnetic drug targeting or magnetic hyperthermia the quantitative knowledge of the MNP distribution inside a body is essential. Several MNP specific imaging modalities (e.g. Magnetic Particle Imaging (MPI) and magnetorelaxometry (MRX)) are potentially able to accomplish this task. A necessary prerequisite for the validation of these imaging modalities in terms of quantitative reproducibility and feasibility under pre-clinical conditions is a suitable phantom with well known properties.

Phantom design

We developed a rabbit sized phantom that was designed according to the experience gained in a previous *in-vivo* MNP imaging study where the therapeutic efficiency of magnetic drug targeting was investigated in rabbit tumor models by MRX. The diamagnetic phantom body made of Plexiglas® (l = 50 cm, b = 40 cm, h = 8 cm) reflects a typical rabbit. Gypsum cubes (1cm^3) homogeneously loaded with MNP serve as basic component to model complex MNP distributions. Two supports inside the phantom (capable to house 320 ($8N_x \times 8N_y \times 5N_z$) MNP loaded cubes) offer the possibility to generate MNP distributions at spatially distinct body regions (tumor region at hind leg and liver-lung region) of a rabbit. Additionally, vessels can be used as well to model MNP injection during drug targeting therapy. Defined drills located at the top and bottom of the phantom guarantee an accurate positioning of marker and/or excitation coils with a fixed position relative to the MNP distribution that shall be investigated in the magnetic measurements. The phantom was used to investigate the quantitative reconstruction of an MNP distribution by spatially resolved MRX.

Conclusion

Our results demonstrate that the phantom is a suitable tool for providing complex and reproducible MNP distributions with defined conditions in terms of geometry and MNP content for validation of MNP imaging techniques preparing the application in pre-clinical environments.

Protein corona formation around magnetic nanoparticles administered into a biological system

A. Weidner Institute of Biomedical Engineering and Informatics (BMTI), Technische Universität Ilmenau, Ilmenau, Germany, andreas.weidner@tu-ilmenau.de
J.H. Clement Klinik für Innere Medizin II, Abteilung Hämatologie und Internistische Onkologie, Universitätsklinikum Jena, Jena, Germany, joachim.clement@med.uni-jena.de
F. v. Eggeling Institut für Physikalische Chemie (IPC), Jena Center for Soft Matter (JCSM) and Institut für Humangenetik, Core Unit Chip Applikationen, FSU und Universitätsklinikum Jena, Jena, Germany, f.v.eggeling@uni-jena.de
F.H. Schacher Institut für Organische und Makromolekulare Chemie (IOMC) and Jena Center for Soft Matter (JCSM), Friedrich Schiller Universität Jena, Jena, Germany, felix.schacher@uni-jena.de
S. Dutz Institute of Biomedical Engineering and Informatics (BMTI), Technische Universität Ilmenau, Ilmenau, Germany, silvio.dutz@tu-ilmenau.de

Introduction

When exposing nanomaterials, e.g. superparamagnetic iron oxide nanoparticles (SPIONs), to the peripheral blood a protein corona is formed immediately. The composition of the formed protein corona might be of major importance for cellular uptake of magnetic nanoparticles. Aim of here presented experiments is to analyze the importance of temperature on the formation of the protein corona during in vitro serum incubation.

Methods

SPIONs were prepared by alkaline precipitation and coated with amino-dextran, dextran, or carboxymethyl-dextran. The obtained core/shell nanoparticles were incubated in fetal calf serum (FCS) at 50°C, 37°C, and 15°C by magnetic heating (hyperthermia) of the SPIONs within FCS or adding the SPIONs to FCS with the desired temperature. The SPIONs were incubated for 15 minutes and then cooled down to room temperature. Before and after incubation physical properties of the particles were determined. Incubated nanoparticles were applied to a TBS polyacrylamide gradient gel under denaturing conditions and protein bands were visualized by Coomassie blue staining. The effect of incubated particles on cell viability was tested for human brain microvascular endothelial cell line (HBMEC) with the PrestoBlue™ Cell Viability Assay.

Results

Results show, that zeta potential is a function of incubation temperature. Thereby it is demonstrated, that incubation temperature has an influence on the composition of the corona. Electrophoretic analysis of the components of the protein corona shows that the predominant protein is serum albumin with its derivatives. SPIONs which were treated with hyperthermia contain more protein than nanoparticles exposed to external heating. Investigated samples have no cytotoxic effect for tested cell lines.

Conclusion

We found very promising results regarding the influence of temperature as well as the type of heating on corona formation. Due to the possibility of heating by magnetic losses (additionally to the external heating) magnetic nanoparticles are very interesting model particles for ongoing investigations.

Acknowledgements: This work was supported by Deutsche Forschungsgemeinschaft (DFG) in frame of priority programme 1681 (FKZ: DU 1293/4-1, EG 102/6-1, SCHA1640/7-1, CL202/3-1) and by Interdisziplinäres Zentrum für Klinische Forschung Jena.

Analysis of viscosity-dependent particle response in the context of Magnetic Particle Imaging

T. Wawrzik, C. Kuhlmann, H. Remmer, M. Schilling, F. Ludwig
Institut für Elektrische Messtechnik und Grundlagen der Elektrotechnik, TU Braunschweig, Braunschweig, Germany
t.wawrzik@tu-bs.de

Introduction

The ability to determine the mobility or binding state of particles in the field-of-view of an Magnetic Particle Imaging (MPI) experiment is key for the realization of in-vivo/-vitro immune assays or the imaging of marker affinity to different cells/tissues and provides an angle towards functional/molecular imaging. We are currently developing a mobility MPI (mMPI) setup to experimentally demonstrate the feasibility of such procedure. Magnetic Particle Spectroscopy (MPS) provides insights into the particle response dynamics and therefore it allows us to perform preparatory experiments towards mMPI.

Methods

In mMPI the dependence of the imaging kernel on viscosity or particle binding state is to be determined. For that the delta response of two or more images (over an accessible imaging parameter, i.e. drive field frequency) is evaluated in comparison with a dynamic particle model. In preparation, for mMPI reconstruction and in order to proof the validity of our models, we analyze the measured particle responses of different viscous samples and compare them with simulated ones obtained with our models.

Results

Magnetic Particle Spectroscopy (MPS) measurements from our multi-frequency MPS are shown and correlation to simulated datasets is validated.

Financial support by the German Federal Ministry of Economics and Technology under grant no. FKZ KF3061201UW2, by the European Commission Framework Programme 7 under the NAMDIATREAM project (NMP-2010-246479) and the NANOMAG project (NMP-2013-604448) as well as by the DFG (LU800/4-1) are acknowledged.

Quantitative biomarker detection with magnetic nanoparticles

Dieckhoff J., Remmer H., Schilling M., Ludwig F.
Institut für Elektrische Messtechnik und Grundlagen der Elektrotechnik, TU Braunschweig, Braunschweig, Germany
f.ludwig@tu-bs.de

Introduction

Functionalized magnetic nanoparticles (MNPs), e.g. iron oxide nanoparticles with a receptor protein covered polymer shell, enable a quantitative detection of biomarkers directly in solution without any wash-out steps. In this work, we report on the realization of such a detection scheme based on the application of rotating magnetic fields.

Methods

The applied MNPs are single-core particles with a 30 nm core diameter (SHP-30 from Ocean Nanotech, USA). The rotating magnetic field is generated with a 2-axis Helmholtz coil system and the response of the MNPs to the field is measured with fluxgate magnetometers. The output signal of the detection scheme is the change of the phase lag $\Delta\varphi$ between the rotating magnetic field and the MNP magnetic moments caused by biomarkers bound to the receptor proteins on the MNP shells. As a test system, the MNPs are functionalized with protein G (IPG-30) which binds specifically to the Fc region of antibodies. Furthermore, the 30 nm MNPs are used to explain the detection of medical relevant biomarkers, e.g. the HER2 protein known from breast cancer diagnosis and therapy.

Results

The phase lag change of the IPG-30 MNPs in a rotating magnetic field possesses a dependency on the antibody concentration in solution that can be well measured and described with a logistic function (calibration curve). Thus, any measured phase lag change can be attributed to the present protein concentration in solution for a given MNP concentration and associated calibration curve.

Conclusion

The measurement of the phase lag change in a rotating magnetic field enables a quantitative detection of proteins with functionalized MNPs direct in solution. Thus a fast, easy to perform and reliable monitoring of biomarkers is possible.

This work was supported by the European Commission Framework Programme 7 under the NAMDIATREAM project (NMP-2010-246479).

Magnetorelaxometry imaging of magnetic nanoparticles with m-sequence based inhomogeneous excitation fields

D. Baumgarten, Institute of Biomedical Engineering and Informatics, Technische Universität Ilmenau, Ilmenau, Germany, daniel.baumgarten@tu-ilmenau.de
Maik Liebl, Physikalisch-Technische Bundesanstalt, Berlin, Germany, maik.liebl@ptb.de

Introduction

The distribution of magnetic nanoparticles can be quantitatively determined from multichannel magnetorelaxometry measurements by least squares techniques. The sequential activation of inhomogeneous excitation fields considerably enhances the imaging quality compared to homogeneous magnetization of the particles. Whereas in first studies single coils were consecutively activated, we recently introduced excitation patterns based on m-sequences involving several excitation coils per measurement.

Methods

Families of m-sequences and random sequences were examined and compared in computer simulations with respect to the condition of the underlying inverse problem. Selected sequences were then employed in magnetorelaxometry imaging experiments with multi-coil excitation. The measurements were obtained with a setup comprising 30 excitation coils and the 304 channel SQUID system at the PTB, Berlin, involving animal-sized phantoms and gypsum cubes with defined nanoparticle concentrations. Imaging results obtained with consecutive activation of single coils and multi-coil excitation patterns based on random sequences and m-sequences were compared.

Results

Simulations yield that the values of the condition number decrease with larger number of measurement samples for all approaches. However, m-sequence based sequences considerably reduce the required number of samples. Two-dimensional and three-dimensional geometrically defined particle distributions could be quantitatively reconstructed from the measurement results obtained with both single-coil and multi-coil excitation patterns. However, a reduction in imaging quality can be observed for patterns with more than 3 coils per measurement.

Conclusion

The obtained results from simulations and experimental measurements indicate that multi-coil excitation patterns allow for a considerable reduction of the number of measurements while preserving the condition of the underlying inverse problem and therewith achieving a comparable imaging quality. Therewith, the overall measurement time can be considerably reduced. Alternatively, magnetization and measurement times can be enlarged for lower detection limits within the same total measurement time.

Analysis and quantification of aggregated nanoparticles by temperature dependent magnetorelaxometry

C. Knopke[1], F. Wiekhorst[1], D. Eberbeck[1], S.Wagner[2], L. Trahms[1]

[1]Physikalisch-Technische Bundesanstalt, Berlin, Germany, christian.knopke@ptb.de
[2]Charité University Medicine, Berlin, Germany

Abstract

To tailor magnetic nanoparticles (MNP) for peculiar biomedical applications qualitative and quantitative information about the particles and their magnetic characteristics is required. In biological environments effects like immobilization and aggregation may alter the magnetic behavior and biomedical functionality of the particles. In this study we deliberately aggregated MNP to examine their magnetic properties applying temperature dependent magnetorelaxometry (TMRX). We found that the underlying interaction process is independent from the macroscopic concentration and thus a well known quantification method could be employed in this case as well.

1 Introduction

Magnetic nanoparticles (MNP) offer a variety of biomedical applications like imaging [1], drug targeting [2] or hyperthermia [3]. These in vivo applications crucially depend on information about quantity and functionality of the MNP. When injected into the bloodstream, particles tend to accumulate in various organs of the organism, such as liver, kidney or spleen [4]. Immobilization and aggregation of MNP may also occur and might drastically change their functionality and biocompatibility [5]. Magnetorelaxometry (MRX) is a technique where the magnetic response of MNP to a step like change of an external field is measured. It is a powerful tool for the quantitative measurement of the nanoparticle amount in vitro as well as in vivo because dia- or paramagnetic tissue gives no MRX signal [6].

2 Methods

A typical MRX sequence consists of two phases. First, a static external field is applied to the sample which aligns the magnetic moments of the MNP. In the second phase the external field is switched off and the magnetic moments return to an equilibrium state. Sensitive magnetic field sensors like SQUIDS or fluxgates measure the decay of the net magnetization.

2.1 MNP samples

For the quantification experiment we used citrate coated iron oxide MNP manufactured by Charité Berlin. We prepared two dilution series from the original particle system (c_{Fe} = 0.1 mol/l) in distilled water for one and sodium chloride solution (1 mol/l) for the forced aggregation.

The addition of sodium chloride leads to visible aggregation after 30 min (Image 1). Both series then were immobilized by freeze drying after addition of 30 µl mannitol(c_{mannit} = 50 mmol/l) solution over night.

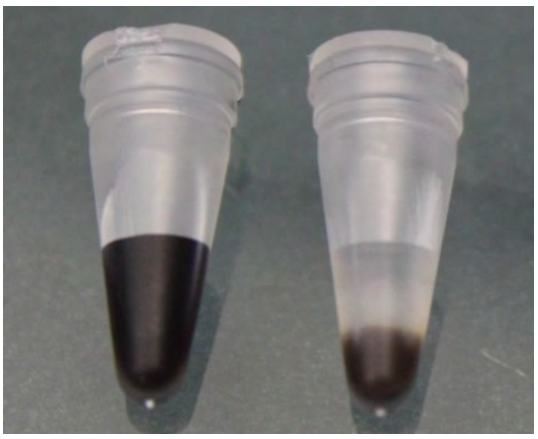

Image 1: visible aggregation after 30 min

2.2 MRX measurement device

For TMRX measurements we utilized a conventional SQUID magnetometer (MPMS-XL, Quantum Design). At fixed temperatures between 10 K and 300 K the samples were magnetized with 1 mT. The removal of the 1 mT field from the superconducting magnet lasted for about 1.5 min during which the SQUID could not be turned on (dead time). This comparatively long dead time (other MRX systems may have a dead time in the microsecond range) requires an elongated magnetization and measurement time. At each temperature the samples were magnetized for 460 s and their relaxation signal measured for 40 min. The TMRX curves were obtained from the decay of the magnetic moment within that measurement time interval. From the relaxation amplitude ($\Delta \boldsymbol{m}$ [Am²]) one may derive the mass magnetization amplitude ($\Delta \boldsymbol{M}$[Am²/g Fe]).

3 Results

For both aggregated and unaggregated systems the temperate of the amplitude maximum $\boldsymbol{T}_{\mathbf{max}}$ is well below room temperature. The forced aggregation through the addition of NaCl solution leads to a change in the relaxation curve shape. The temperature of the amplitude maximum went up from 130 K for not aggregated particles to 210 K for the aggregated system [Image 2]. This shift results from a higher magnetic viscosity which may be attributed to higher energy barriers.

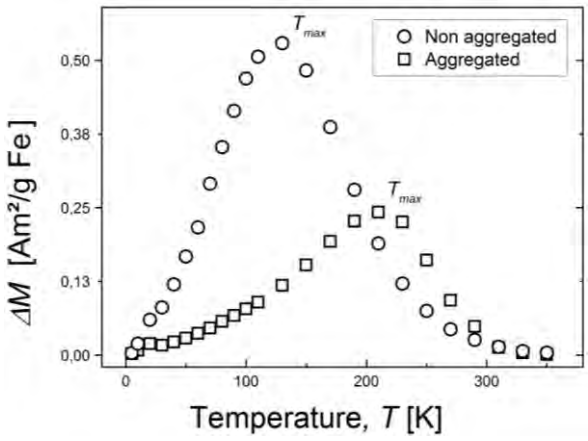

Image 2 Change in TMRX curve due to aggregation

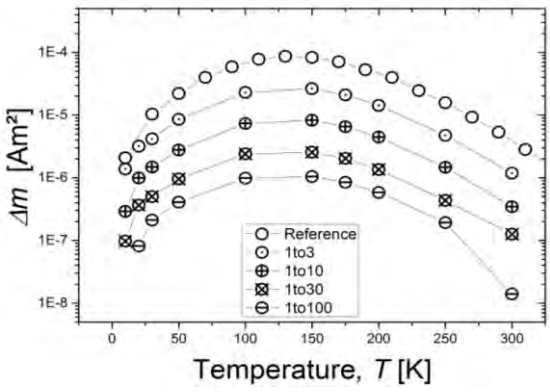

Image 3 Change of TMRX signal of not aggregated particles due to dilution

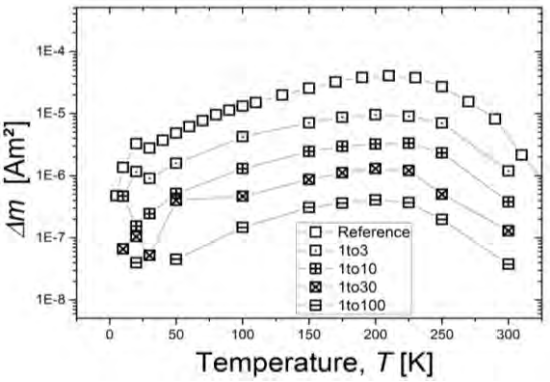

Image 4 Change of TMRX signal of aggregated particles due to dilution

The dilution did not change the curve shape or maximum temperature [Image 3 and 4] which indicates a constant relaxation time. This is contrary to other studies where $\boldsymbol{T}_{\mathbf{max}}$ scales with the concentration [7]. Also, the decrease of the amplitude is directly proportional to the nominal iron content within the samples [Image 5].

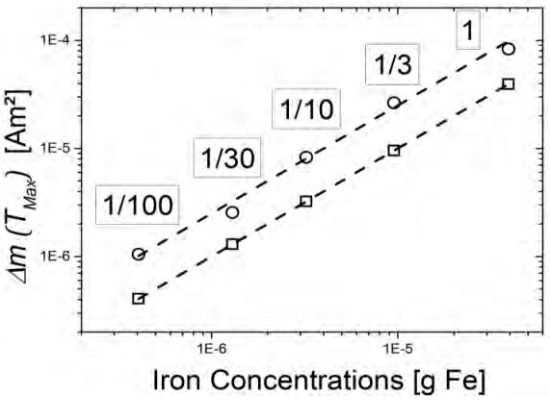

Image 5 Nominal total iron amount versus measured relaxation amplitude at the maximum temperature for aggregated (circle) and not aggregated particles (square)

Thus, the iron content of a sample may be determined using a known reference sample having the same TMRX curve shape [8]. Note that quantification by TMRX is reliable only if the curve shape of the TMRX spectra remains unchanged.

4 Conclusion

TMRX reveals detailed information about the magnetic behavior of MNP: in the present study aggregation leads to an increase of the temperature of the amplitude maximum. This may be attributed to dipole-dipole-interaction: the aggregated particles have a smaller average core to core distance which increases the interaction energy, here slowing down the particles' relaxation.

On the other hand, the dilution series reveals that the magnetic relaxation signals scale linearly with the macroscopic concentration implying that the underlying interaction process is independent on it. Hence the dipole-dipole-interaction is attributed to the local MNP superstructure, i.e. cluster architecture.

5 Acknowledgment

This work was financially supported by the DFG research program KFO 213 „Magnetische Nanopartikel für die Zelluläre und Molekulare MR-Bildgebung" (TR408/5-2), and the DFG priority program 1681(TR408/8-1).

6 References

[1] Wuerfel, Eva, et al. "Electrostatically Stabilized Magnetic Nanoparticles–An Optimized Protocol to Label Murine T Cells for in vivo MRI." *Frontiers in neurology* 2 (2011).

[2] Seeney, Charles, et al. "Magnetically vectored platforms for the targeted delivery of therapeutics to tumors: history and current status." *Nanomedicine*7.2 (2012): 289-299.

[3] Ahmed, Naveed, Hatem Fessi, and Abdelhamid Elaissari. "Theranostic applications of nanoparticles in cancer." *Drug discovery today* 17.17 (2012): 928-934.

[4] Khlebtsov, Nikolai, and Lev Dykman. "Biodistribution and toxicity of engineered gold nanoparticles: a review of in vitro and in vivo studies." *Chemical Society Reviews* 40.3 (2011): 1647-1671.

[5] Soto, Karla, K. M. Garza, and L. E. Murr. "Cytotoxic effects of aggregated nanomaterials." *Acta Biomaterialia* 3.3 (2007): 351-358.

[6] Wiekhorst, Frank, et al. "Magnetorelaxometry assisting biomedical applications of magnetic nanoparticles." *Pharmaceutical research* 29.5 (2012): 1189-1202.

[7] Zhang, Jinlong, C. Boyd, and Weili Luo. "Two mechanisms and a scaling relation for dynamics in ferrofluids." *Physical review letters* 77.2 (1996): 390.

[8] Knopke, Christian, et al. "Quantification of Magnetic Nanoparticle Uptake in Cells by Temperature Dependent Magnetorelaxometry." *Magnetics, IEEE Transactions on* 49.1 (2013): 421-424.

New Methodology for the Forward Problem in EEG/MEG Source Analysis and in Brain Stimulation

Vorwerk, J.[1], Wagner, S.[1], Aydin, Ü.[1], Engwer, C.[2], Wolters, C.H.[1]
[1]Institut für Biomagnetismus und Biosignalanalyse, Westfälische Wilhelms-Universität Münster, Münster, Germany
[2]Institut für Numerische und Angewandte Mathematik, Westfälische Wilhelms-Universität Münster, Münster, Germany

j.vorwerk@uni-muenster.de

Introduction

Besides solving the EEG/MEG forward problem, the accurate simulation of the electric potentials and currents in the human head using highly realistic volume conductor models has recently emerged interest in the optimization/understanding of brain stimulation techniques such as tDCS or TMS. Here, source simulation and brain stimulation are directly linked via the Helmholtz reciprocity principle, so that the obtained insights, e.g. with regard to volume conduction effects, can be transferred between these modalities.

Methods/Results

We apply finite element methods (FEM) for both EEG/MEG forward simulations as well as for tDCS simulations, since they offer the possibility to easily include complex geometries at a reasonable computational complexity and thereby allow for the use of highly realistic head models [1].
We investigate the effects of volume conduction on EEG/MEG forward solutions, identifying the most important conductive compartments to be modelled as well as the most affected brain areas. Evaluating measurement data of an epilepsy patient, we demonstrate the practical benefit of a simultaneous analysis of EEG and MEG, as well as the importance of highly realistic head modelling [2]. In contrast to EEG/MEG forward simulations, where one is mainly interested in the accurate simulation of signal topography and magnitude, the interest in tDCS simulations focuses on the current strength and orientation in a target area [3]. We present ways to optimize the current flow – and thereby the expected stimulation – both with regard to amplitude and orientation in a focal target area.
Despite the generally high accuracy of the used FEM approaches, there are some limitations which have to be taken into account and might complicate the creation of highly realistic head models. We present a new approach based on Discontinuous Galerkin Methods, which – amongst other features – circumvents these problems and might allow for an easier construction of volume conductor models [4].

Acknowledgements: This research was supported by the German Research Foundation (DFG), projects WO1425/2-1, 3-1, 5-1.

[1] S. Lew, C. H. Wolters, T. Dierkes, C. Röer, and R. S. MacLeod, "Accuracy and run-time comparison for different potential approaches and iterative solvers in finite element method based EEG source analysis," *Appl. Numer. Math.*, vol. 59, no. 8, pp. 1970–1988, Aug. 2009.
[2] Ü. Aydin, J. Vorwerk, P. Küpper, M. Herrs, H. Kugel, A. Galka, L. Hamid, J. Wellmer, C. Kellinghaus, S. Rampp, and C. H. Wolters, "Conbining EEG and MEG for the reconstruction of epileptic activity using a calibrated realistic volume conductor model," *Plos One*, Accepted for publication.
[3] S. Wagner, S. M. Rampersad, Ü. Aydin, J. Vorwerk, T. F. Oostendorp, T. Neuling, C. S. Herrmann, D. F. Stegeman, and C. H. Wolters, "Investigation of tDCS volume conduction effects in a highly realistic head model," *J. Neural Eng.*, vol. 11, no. 1, p. 016002, Feb. 2014.
[4] J. Ludewig, "Discontinuous Galerkin Methods for the EEG forward problem," Master Thesis, University of Münster, 2013.

Reliable Fast Adaptive Finite Element Methods for the EEG/MEG Forward Problem

A.Hanrath, Institute for Geometry and Practical Mathematics (IGPM), RWTH–Aachen, Germany, *hanrath@igpm.rwth-aachen.de*
L.Grasedyck, Institute for Geometry and Practical Mathematics (IGPM), RWTH–Aachen, Germany, *lgr@igpm.rwth-aachen.de*

Introduction

The Solution of the EEG-forward problem with Finite Element Methods (FEM) was recently studied, e.g. Wolters et al 2007, Lew et al 2009 or Schimpf et al. 2002. Such methods are good when dealing with inhomogenous materials. One drawback is that an enormous amount of computational power is needed to compute with high-resolution headmodels.
To reduce this amount significantly we propose to use Adaptive Finite Element Methods (AFEM). These use the high resolution only where it is needed. The refinement is steered by reliable error estimators.

Methods

We compared the standard AFEM proposed by Binev, Dahmen and DeVore 2004 or Stevenson 2007, which reduces the L2-error on the whole domain, with a goal oriented AFEM (GoAFEM) proposed by Mommer and Stevenson 2009 on reality oriented geometries.
In the context of the EEG/MEG-forward-problem the goal is to minimize the error at the sensor positions.
The first step is to take care of the singularities in the right-hand side and the goal functional. We use the blurred dipole Ansatz proposed by Buchner et al. 1997 to regularize the right-hand side as well as the goal-functional.
After this regularization a gradient based estimator is used.

Results

Adaptive refining without using the goal functional leads to strong local refinement around the dipoles position. This has almost no effect for the solution at the sensor positions. Also just refining around the sensor positions leads to no improvement at all.
The best results are given if the area around the dipole and the sensors as well as the space between them is accurately resolved.

Conclusion

Adaptive refinement works rather well if all kinds of Adaptivity are taken into account and balanced. We therefore propose to use the GoAFEM to reduce the high resolution of head models.

Realistic modelling of skull defects in finite element head models for source reconstruction from MEG and EEG

S. Lau, Institute of Biomedical Engineering and Informatics, Faculty of Computer Science and Automation, Technische Universität Ilmenau, Germany, stephan.lau@tu-ilmenau.de; Biomagnetic Center, Department of Neurology, Jena University Hospital, Jena, Germany; Department of Electrical & El. Engineering and Department of Medicine – St. Vincent's Hospital, University of Melbourne, Parkville, Australia;

D. Güllmar, Medical Physics Group, Department of Diagnostic and Interventional Radiology, Friedrich-Schiller-University Jena, Germany, daniel.guellmar@med.uni-jena.de

L. Flemming, Biomagnetic Center, Department of Neurology, Jena University Hospital, Jena, Germany

J. Haueisen, Institute of Biomedical Engineering and Informatics, Faculty of Computer Science and Automation, Technische Universität Ilmenau, Germany, jens.haueisen@tu-ilmenau.de

Introduction

The influence of skull defects on the MEG and EEG signals recorded above the skull defects was recently determined to be substantial using an in vivo animal experiment [1]. Our objectives are to describe errors in source reconstruction from MEG and EEG signals due to ignoring skull defects and to recommend modelling steps for skull defects in FE head models.

Methods

We constructed a complete finite element (FE) simulation of an in-vivo animal experiment with a skull defect above a controlled source [1]. The body, ocular humour and lens, compact and cancellous bone, skull defects and grey matter, white matter, CSF and intracranial blood vessels were segmented from a T2 MRI (0.4 mm^3) and a co-registered CT (0.4 mm^3). A nodeshifted cubic mesh was derived (Vgrid). The 64-channel EEG and the 16-channel MEG were forward simulated using the blurred dipole approach (SimBio). Source reconstruction from the MEG and EEG recordings respectively was performed using an unconstrained moving dipole fit (SimBio).

Results

Sources under a skull defect reconstructed from MEG signals with an intact skull model were displaced away from the defect. Sources next to the skull defect were reoriented. Sources under a skull defect reconstructed from the EEG signals with an intact skull model were displaced towards the defect and oriented to point ot the defect. When the sources were instead reconstructed with a head model incorporating the skull defects, the displacement was non-linearly reduced as the modelled defect conductivity approached the experimental conductivity and the dipole orientation was gradually restored.

Conclusion

Modelling skull defects substantially reduces their impact on source reconstruction from MEG as well as EEG signals. The skull defect boundary and conductivity should be modelled as accurate as possible. Accurate FE method based head modelling incorporating skull defects can improve localisation of brain activity.

References

[1] Lau S., Flemming L., Haueisen J. Magnetoencephalography signals are influenced by skull defects. Clin Neurophysiology 2014 [Epub ahead of print].

Influence of the head model on EEG and MEG source connectivity analysis

J.-H. Cho[1*], J. Vorwerk[2], C.H. Wolters[2], T.R. Knösche[1]
[1]Max Planck Institute for Human Cognitive and Brain Sciences, Leipzig, Germany
[2]Institute for Biomagnetism and Biosignalanalysis, University of Münster, Münster, Germany

[*]jhcho@cbs.mpg.de

Introduction

The present study examines the influence of the head model on source connectivity analysis in EEG and MEG. In particular, we investigated the effects of the inclusion of separate compartments for white/grey matter, hard/spongy bone and cerebrospinal fluid (CSF).

Methods

As a reference, a detailed finite element head model was created, comprising six layers: skin, hard/spongy bone, CSF, and white/grey matter. Four test models were derived from that reference model to consider the effects of particular simplifications: ignoring white/grey matter distinction, ignoring hard/spongy bone distinction, not modeling CSF, and reduction to a 3-layer model (skin, skull, and brain). The source space was placed inside the grey matter with surface normal orientation. For connectivity simulation, we assumed a two-source scenario in which one source is fixed at one position and the other source is sequentially located at all other positions. The information flow was set from source 1 to 2. The dynamics were simulated using a neural mass model. An LCMV beamformer was used for source reconstruction, while imaginary coherence (IC) and generalized partial directed coherence (GPDC) were used as connectivity measures. The connectivity results were compared using the relative error between the results from the original and reconstructed signals.

Results

Our results show that neglecting white/grey matter distinction and CSF mainly affect the reconstructed signals and their connectivity analysis. Large inverse and connectivity errors are found in certain regions showing large topography errors in forward solution. The IC is less affected by the cross-talk effect and yields lower and more spatially restricted errors than the GPDC.

Conclusion

We conclude that the white/grey matter distinction and the CSF compartment should be included in head modeling to reduce the inverse error and the cross-talk effect caused by an imperfect head model on source connectivity analysis in both EEG and MEG.

Skull-equivalent material for an EEG physical head phantom

A. Hunold, Institute of Biomedical Engineering and Informatics, Faculty of Computer Science and Automation, Technische Universität Ilmenau, Germany, alexander.hunold@tu-ilmenau.de

P. Fiedler, Institute of Biomedical Engineering and Informatics, Faculty of Computer Science and Automation, Technische Universität Ilmenau, Germany, patrique.fiedler@tu-ilmenau.de

S. Lau, Institute of Biomedical Engineering and Informatics, Faculty of Computer Science and Automation, Technische Universität Ilmenau, Germany, stephan.lau@tu-ilmenau.de; Biomagnetic Center, Department of Neurology, Jena University Hospital, Jena, Germany

D. Güllmar, Medical Physics Group, Department of Diagnostic and Interventional Radiology, Friedrich-Schiller-University Jena, Germany, daniel.guellmar@med.uni-jena.de

J. Haueisen, Institute of Biomedical Engineering and Informatics, Faculty of Computer Science and Automation, Technische Universität Ilmenau, Germany, jens.haueisen@tu-ilmenau.de

Introduction

Physical head phantoms allow for the assessment of EEG source reconstruction procedures and electrical stimulation profiles during transcranial current stimulation. Especially, the skull representing the main conductivity barrier influences the electric potential distribution in the head. In the present study we aim to select a suitable material to physically model the human skull.

Methods

The requirements for the physical head phantom are an electrolyte conduction on a physiological conductivity level as well as formability and reuseability. Plastic clay provided formability and was permeable for ions in general. Five clay types varying in granularity and fractions of fireclay, annealed (pottery) with firing temperatures from 550°C to 950°C, were analysed regarding their conductivity when emersed in an electrolyte solution. Four-point impedance measurements across pottery samples in sodium-chloride solution (0.9%) were conducted and the conductivity was determined based on the known geometry. The pottery samples were cleaned and the impedance measurements repeated to test the reuseabilty of the skull material.

Results

Within the set of the analysed pottery samples the conductivity varied between 0.0716 S/m and 0.0224 S/m. The diffusion of ions in the clay probe resulted in a time-dependend impedance evolution during the first approx. 30 min after exposure to the sodium-chloride solution. The agglomeration of sodium-chloride in the pottery samples was successfully washed out in a rinsing procedure. The pottery samples provided reproducible conductivity properties.

Conclusion

The clay type with the minimal conductivity of 0.0224 S/m represented a suitable skull conductivity. Clay pottery is a suitable skull-equivalent material for the construction of a realistic physical head phantom.

Towards an automated method of generating volume conductor models

D. Portain, H. Sonntag & B. Maess

Max Planck Institute for Human Cognitive and Brain Sciences, Leipzig, Germany, portain@cbs.mpg.de

Introduction

Accurate bioelectro-magnetic forward modeling also relies on precise construction of individual volume conductors. Realistic volume conductor models are derived from a segmentation of structural MRI data sets. We propose an procedure that creates models by combining T1- and T2*-weighted MRI data of our subjects without manual intervention. The procedure consists of several steps: denoising, bias field correction, tissue classification and compartment construction.

Materials and Methods

Denoising of the T1- and T2*-weighted datasets is performed by an adaptive, non-local means denoising method with spatially varying noise levels (Manjon and Coupé, 2010). Bias field correction and the tissue classification are performed by a fully multispectral variant (Alonso, 2011) of the unified segmentation in SPM12b (Ashburner and Friston, 2005). The resulting individual tissue probability maps are compartmentalized using distance regularized level set evolutions (DRLSEs; Li et al., 2010). Grey and white matter segmentation is supplied by Freesurfer. Anatomical plausibility is evaluated from tissue topology and volume ratios. If necessary, tissue topology violations (e.g., neighboring CSF and skin voxels) are resolved by relabeling individual voxels.

Results

Compartment construction with the simple Maximum-Likelihood (ML) approach is sensitive to noise resulting in tissue fragmentation. Fragmentation leads to anatomically less plausible models, and may introduce leaks in thin layers. Compensating for tissue fragmentation requires multiple post-processing steps or even manual intervention. Denoising and the DRLSE approach together resulted in non-fragmented compartments for skin and skull layers. Our procedure was developed using real data of two individuals and tested with data of fifteen individuals. Final models show no topology errors in the skull compartment. Compared to ML, our approach yields no systematic change in tissue volume, but a 30% smaller skull compartment.

Conclusion

We show that a fully automated procedure produces anatomically plausible, 5-compartment volume conductor models for healthy adults based on T1- and T2*-weighted MRI datasets.

Simulation of magnetic nanoparticle interactions in magnetic drug targeting models

C. Gordalla (1), A. Roeth (2), T. Schmitz-Rode (1), M. Baumann (1), I. Slabu (1, 3)

(1) Applied Medical Engineering, Medical Faculty, Helmholtz Institute, RWTH Aachen University, Germany
(2) Department of General, Visceral and Transplantation Surgery, University Hospital Aachen, Germany
(3) Physikalisch-Technische Bundesanstalt, Berlin, Germany

Introduction

Magnetic drug targeting (MDT) describes the selective targeting of therapeutics bound to magnetic nanoparticles (MNP) in a tissue or a region in the body, e. g. in a tumor, by magnetic fields. For an efficient tumor therapy with MDT, it is important that significant amounts of the drugs bounded to MNP reach the tumor site. In order to predict the accumulated amount of MNP, FEM simulations of the behavior of magnetic nanoparticles in blood flow under the influence of a magnetic field were performed. The physical and chemical properties of the MNP as well as interactions between different kinds of MNP were taken into account.

Methods

Simulations of a capillary blood flow with suspended MNP under the influence of magnetic fields were performed with the software Comsol Multiphysics using the finite element method (FEM) and backward differentiation formulae (BDF). The simulations describe the influence of MNP interactions, such as steric repulsion, van der Waals attraction, dipole-dipole interactions and interactions with the magnetic fields, on the adsorption rate of the MNP at the capillary wall for different kinds of MNP and different magnetic field configurations.

Results

The highest predicted adsorption rate within one hour at the capillary wall is of approx. 20 % of the MNP total amount flowing through the capillary. This value is predicted for an MNP concentration of 0.1 mg/l, an average blood velocity of 0.03 cm/s, and a magnetic field with maximum field strength of 1.35 T and a maximum gradient of 2000 T/m. Furthermore, the simulated steric repulsion of the MNP causes the strongest influence on the increase of the MNP adsorption rate at the capillary wall.

Conclusion

Significant development of MDT prediction models was achieved by implementation of MNP interactions into the simulations which helps to improve the effectiveness of current MDT tumor therapy.

Detection limits of SPIO loaded mesh implants for visualization in MRI and MPI

M. Ariens (1), F. Wiekhorst (2), T. Schmitz-Rode (3), M. Baumann (3), C. Kuhl (1), C. Liess (4), L. Trahms (2), I. Slabu (2, 3)

(1) Department of Radiology, University Hospital Aachen, Germany
(2) Physikalisch-Technische Bundesanstalt, Berlin, Germany
(3) Applied Medical Engineering, Medical Faculty, Helmholtz Institute, RWTH Aachen University, Germany
(4) Philips Healthcare, Hamburg, Germany

Introduction

The concept of a mesh implant that is visible in MRI and MPI is realized by compounding superparamagnetic iron oxides (SPIO) into the material of the implant. The relation between the amount of SPIO in the implant and the respective R2* relaxivity values was investigated by means of MRI relaxometry. Furthermore, a detection limit for MPI contrast was estimated by measuring the SPIO concentration in the mesh implant using magnetic particle spectroscopy (MPS).

Methods

Both, self-synthesized and commercially available SPIO were integrated at different concentrations into the base material PVDF of threads which were used to knit the mesh implants. For each manufactured thread type and SPIO concentration, the R2* relaxivity in dependence of the SPIO concentration was investigated with a 1.5 T MRI device, and, additionally, the MPS signal was measured. The induced susceptibility difference of each SPIO loaded thread was determined from the hyperintense areas in the MR image as a function of SPIO concentration and thread thickness.

Results

Significant SPIO concentration dependent changes in the R2* relaxivity measurements were observed with R2* relaxivity values ranging from $30\ s^{-1}$ to $40\ s^{-1}$ and induced a susceptibility difference between 2.3 ppm/(mg/g) to 4 ppm/(mg/g). The lowest investigated SPIO concentration in threads which lead to a significant signal in MRI was 1 mg/g. The commercial SPIO caused stronger relaxivity changes and susceptibility differences which can be explained by their bigger SPIO crystal size and higher magnetization values. The MPS measurements revealed a linear dependency of the MPS signal amplitude with the SPIO content, and an MPS detection limit of 0.01 mg/g SPIO concentration was estimated.

Conclusion

The applied methods are a feasible approach to estimate the detection limit of mesh implants in MRI and MPI and to support the optimization process in the development of various mesh implant types.

Using ultra low field nuclear magnetic resonance (ULF NMR) with a one-dimensional vertical phase encoding for direct neuronal current detection

N.H., Höfner, Physikalisch-Technische Bundesanstalt, Berlin, Germany, nora.hoefner@ptb.de

R.K., Körber, Physikalisch-Technische Bundesanstalt, Berlin, Germany, rainer.koerber@ptb.de, Magnicon GmbH, Berlin, Germany

J.H., Haueisen, Institute of Biomedical Engineering and Informatics, Ilmenau University of Technology, Ilmenau, Germany, jens.haueisen@tu-ilmenau.de

M.B., Burghoff, Physikalisch-Technische Bundesanstalt, Berlin, Germany, martin.burghoff@ptb.de

Introduction

The utilization of NMR in the ULF regime could open up the opportunity to detect neuronal activity directly and potentially enhance the spatial resolution limit (~1 cm) of established methods like electroencephalography or magnetoencephalography. Until now in-vitro measurements have been performed.

Methods

A head phantom with an integrated current dipole, in order to imitate neuronal activity, and filled with an aqueous solution serves as a human head. We first focus on the detection of long lasting current dipole moments, which generate an additional local magnetic field during the induced precession of the hydrogen nuclear magnetic moments and thereby alter the NMR signal shape. The measuring sequence starts with the application of a strong magnetic field (~ 50 mT) in order to generate a measurable magnetization within the aqueous solution of the phantom. Thereafter, a fast change to an orthogonal oriented detection field (~ 10 μT) induces a free precession decay (FPD). A DC-SQUID current sensor connected to a first order gradiometer is used to read out the FPD signal. Since we found that a cancellation effect prevents the detection of typical current dipole moments (up to 50 nAm) of human long lasting activities, a spatial encoding in vertical direction is needed.

Results

Removing a part of the phantom volume in order to emulate a spatial encoding in vertical direction and so maintaining the signal to noise ratio, allowed the detection of current dipole moments as low as ~ 70 nAm. However, after integrating a one dimensional phase encoding the resolution limit rose up to ~1 μAm.

Conclusion

The reason is attributed to image distortions resulting from the use of Fourier based reconstruction techniques in the presence of strong concomitant gradients. Thus, the application of post processing algorithms and an adjustment of the measurement sequence should enhance the resolution limit.

Multichannel MEG with microfabricated optically-pumped magnetometers

T.H. Sander[1], O. Alem[2,3], J. Kitching[2], L. Trahms[1], S. Knappe[2,3]
[1] Physikalisch-Technische Bundesanstalt, Berlin, Germany
[2] National Institute of Standards and Technology, Boulder, USA
[3] University of Colorado, Boulder, USA

tilmann.sander-thoemmes @ptb.de

Introduction

Optically pumped magnetometers (OPM) for the measurement of weak magnetic fields in the femtotesla range have been developed in the last decade. Applications such as magnetocardiography and magnetoencephalography with individual or a few channels have been realised. Here the measurement of MEG with an array of 21 microfabricated (μ) OPMs will be discussed.

Methods

Individual μOPMs of 1 cm^2 footprint were assembled into an array consisting of 21 sensors. The sensors were inserted into pre defined openings in a hemispherically shaped holder fitting a subjects head. The sensors were placed mainly on the left hemisphere to cover the area around C3. Raw μOPM data of the subject were recorded during electrical medianus nerve stimulation at the right wrist. Each μOPM incorporates its own modulation coil pair for lock-in detection of the magnetic field. A software lock-in technique was used to obtain the MEG data from the raw μOPM data.

Results

Averaging over 4700 recorded biomagnetic signals after repetitive wrist stimulations yields the typical N20m response occurring 20 ms after the stimulus. Mapping the data from the 21 sensors at the time point of the N20m response a dipolar pattern was observed, which is the expected structure of a N20m response.

Conclusion

It has been demonstrated that miniaturization of OPM sensors allows to design a sensor array suitable to fit the human head and to obtain true multi-channel OPM MEG data. Although μOPMs do not match yet the bandwidth and noise properties of SQUID sensors they can already complement SQUID based MEG arrays by allowing a flexible positioning.

Single-Sided Magnetic Particle Imaging Scanner: System Matrix Measurement

K. Gräfe[1], G. Bringout[1], M. Graeser[1], T. F. Sattel[2], T. M. Buzug[1]
[1] Institute of Medical Engineering, University of Lübeck, Lübeck, Germany, {graefe, buzug}@imt.uni-luebeck.de
[2] Philips Medical Systems DMC GmbH, Hamburg, Germany

Abstract

Magnetic Particle Imaging (MPI) is a new medical imaging method, first presented by Gleich and Weizenecker in 2005. Since then, different scanner designs have been published. In 2009 Sattel et al. presented an innovative single-sided scanner topology. It has the advantage of an unlimited patient access. The MPI process in general, is based on the excitation of super-paramagnetic iron oxide nanoparticles by a sinusoidal varying magnetic field. Additionally, a selection field is generated, which induces a field-free point (FFP). The FFP enables spatial encoding, since only SPIONs in the FFP and its direct neighbourhood generate a significant magnetisation dynamics, which is high enough to be recorded. In this contribution, the measured system matrix of a second-generation oil cooled single-sided scanner is presented, and a first technical validation of the penetration depth is performed.

1 Introduction

Advantages of Magnetic Particle Imaging (MPI) in general are real time imaging capability, high sensitivity, and high spatial resolution [1]. To acquire an image with this technique, tracer material needs to be administered to the scanned object. It consists of super-paramagnetic iron oxide nanoparticles (SPIONs) and has a nonlinear magnetisation characteristic. Due to the excitation of the SPIONs by a sinusoidally varying magnetic field (drive field) the particle magnetisation $M(t)$ changes and a voltage signal u is induced in the receive coil [2]. The signal spectrum $\hat{u}$ is obtained by Fast Fourier Transform (FFT). It contains the fundamental frequency of the drive field and higher harmonics, which are caused by the nonlinearity of the SPIONs. For spatial encoding, a field free point (FFP) is generated. The FFP emerges by the superposition of two magnetic fields, generated by two concentric circular coils with opposite directions of the direct currents (DC).

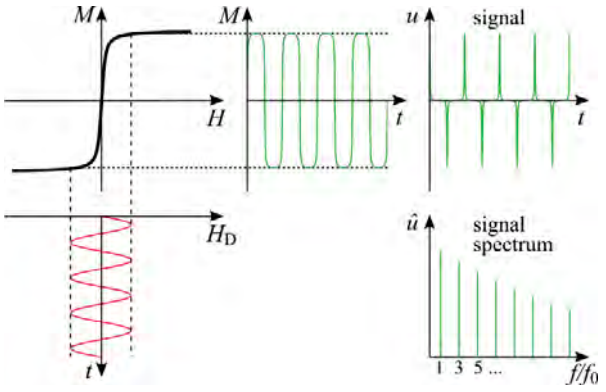

Image 1 The excitation and the magnetisation response of the SPIONs, which lie in the FFP (after [2]).

The FFP is moved by superimposed drive fields on a given trajectory through the field of view (FOV). Only SPIONs in or in the direct vicinity of the FFP are excited by field variation (Image 1).
The SPIONs outside the FFP are in saturation and do not induce a signal in the receive coil (Image 2).

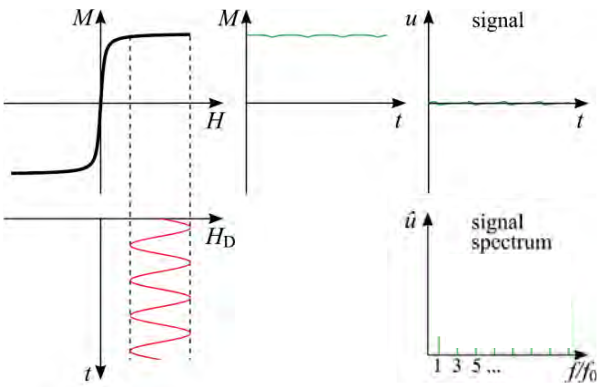

Image 2 The excitation and the magnetisation response of the SPIONs, which lie outside the FFP (after [2]).

The quality of the signal, in terms of amplitude and noise is of particular importance to achieve an acceptable imaging resolution and sensitivity. Thus, analogue filter steps are mandatory.
At the receive chain an analogue band block filter is used for damping the signal of the drive field, which directly couples into the receive coils. Consecutively, a low noise amplifier (LNA) is used to scale the receive-coil signal to the input level of the data acquisition system (DAS).

1.1 Single Sided MPI Scanner

Most MPI scanners are based on a symmetric coil assembly and have a limitation in patient access [1, 2, 3, 4, 5]. The advantage of an asymmetric single sided scanner is that all necessary coils are on one side of the patient [6]. The main disadvantage of this scanner design, however, is its limited penetration depth. Indeed, as the magnetic fields

amplitude and gradient decrease with the distance to the scanner, so do the sensitivity and the resolution.
A medical application scenario for the single-sided scanner is the sentinel lymph node biopsy [7]. In comparison to current lymph node localisation methods, MPI does neither use any high energy radiation nor radioactive tracer material. For this medical application, the limited penetration depth is not seen as a disadvantage, as the lymph nodes lay near to the skin.
The single-sided scanner for one-dimensional imaging consists of two concentrically arranged circular coils (Image 3).

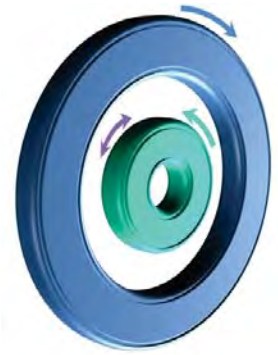

Image 3 Single-sided scanner for one-dimensional imaging. The arrows indicate current directions.

Both coils are carrying DC of opposite directions and generate the selection field. An alternating current (AC) on the inner coil generates the drive field. Image 4 shows the magnetic fields generated by the inner coil (cyan), the outer coil (blue) and the superposition of the two magnetic fields (green). The blue band shows the scanner position and it can be seen that two FFPs are generated: one in front, and a spurious one on the backside of the scanner. For the image acquisition only the front-side FFP is used. However, the drive field will move both FFP.

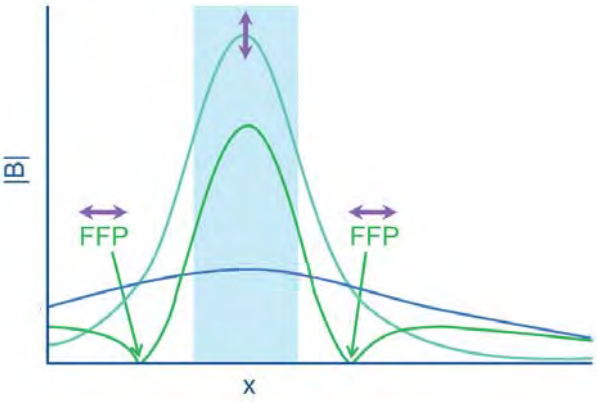

Image 4 Magnetic fields generated by the inner coil (cyan), the outer coil (blue), and the superposition of the two magnetic fields (green). The light blue band shows the scanner position and the violet arrows indicate the movement, caused by the AC on the inner coil.

2 Methods

2.1 System Matrix Measurement

To measure the system matrix a DC of 56 A is applied on the outer coil and 65 A is applied on the inner coil, respectively. An AC current of 42 A is applied on the inner coil. The excitation frequency is 25.252 kHz. To avoid overheating, the scanner has to be oil cooled.
To record the system matrix a quadratic 2 mm x 2 mm x 2 mm sample was filled with 8 µl undiluted Resovist®. The sample has been moved away from the scanner surface in 2 mm steps. The construction shown in image 5 was used to position the sample. Each turn of the nut leads to a 1 mm translation in the x direction. The acquired FOV is 30 mm in x-direction.

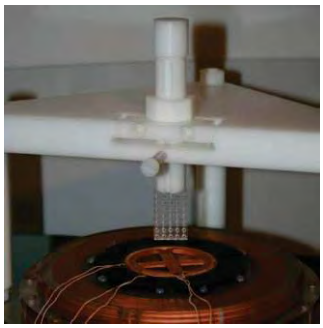

Image 5 Experimental set-up to measure the one-dimensional system matrix. By turning the nut it is possible to translate the sample in the x direction.

Before the receive signal reaches the data acquisition card it is necessary to filter out the main frequency and to amplify the signal with a low noise amplifier. The received signal is amplified by a factor of 500.

2.2 Reconstruction

Before the linear equation (1), for the reconstruction process, can be solved it is necessary to calculate the signal-to-noise ratio (SNR) of the measurement. Therefore, between each particle measurement one empty measurement is acquired and two empty measurements are interpolated. These interpolated values are subtracted from the particle measurement and the root-mean square value over all empty measurements is used to calculate the SNR.
For the reconstruction process only the frequencies with an SNR higher than 10 are used.
To be able to reconstruct the measurement it is necessary to solve the invers problem (1).

$$\hat{S}c = \hat{u} \tag{1}$$

Equation (1) shows the connection between the system matrix, $\hat{S}$, in frequency space, the vector of the particle concentration, c, and the vector of the induced signal frequency components, $\hat{u}$. Generally, equation (1) poses an ill-posed problem, thus the Tikhonov regularization method is applied to solve it. Furthermore, a weighting matrix,

W, [8], a regularization parameter, λ, the identity matrix, I, and the hermitian of the system matrix, $\hat{S}^H$, is added. The weighting matrix is a diagonal matrix and can be calculated by the row energy of the system matrix [8]. In order to solve the ill-posed problem, the linear equation

$$(\hat{S}^H W \hat{S} + \lambda I)c = \hat{S}^H W \hat{u}$$

has to be solved. An adaptive iterative Kaczmarz algorithm [9] is used to solve the system. However, after each iteration the negative values were set to zero and only the real part is used for the reconstruction [10].

3 Results

Image 6 shows the result of the reconstruction of the system matrix. The sample is moved away in 2 mm steps from the single-sided scanner surface.

The lambda values represents the used regularization parameter, the position of the sample probe is given on the ordinate. On each image the single-sided scanner is positioned at the bottom. The maximum distance between the single-sided scanner surface and the particle sample is 28 mm. It can be seen that with increasing distance to the scanner the resolution decrease.

4 Conclusion

With the measurements shown in this work, it has been demonstrated that with an oil-cooled single-sided scanner a FOV in the direction of the scanner access of 30 mm is feasible. The decreasing of the magnetic fields with an increasing distance to the scanner, due to the asymmetric scanner design, caused a degrading resolution. Furthermore, it could be observed, that the efficiency of oil-cooling system is appropriate to achieve stable coil temperature. This is especially important for future measurements, because only with a temperature-drift stable system different measurements can be calibrated to achieve a quantitative imaging result.

It has to be kept in mind that the reconstruction presented here has been carried out under optimal conditions, as the system matrix itself was used for the reconstruction process. If real images in phantom measurement will be reconstructed it will be more difficult to solve the mathematical problem correctly. However, this first study gives a hint for future measurements and the reachable penetration depth within the application scenario.

In future, phantom measurements will be carried out and the single-sided scanner will be extended to a two-dimensional imaging device.

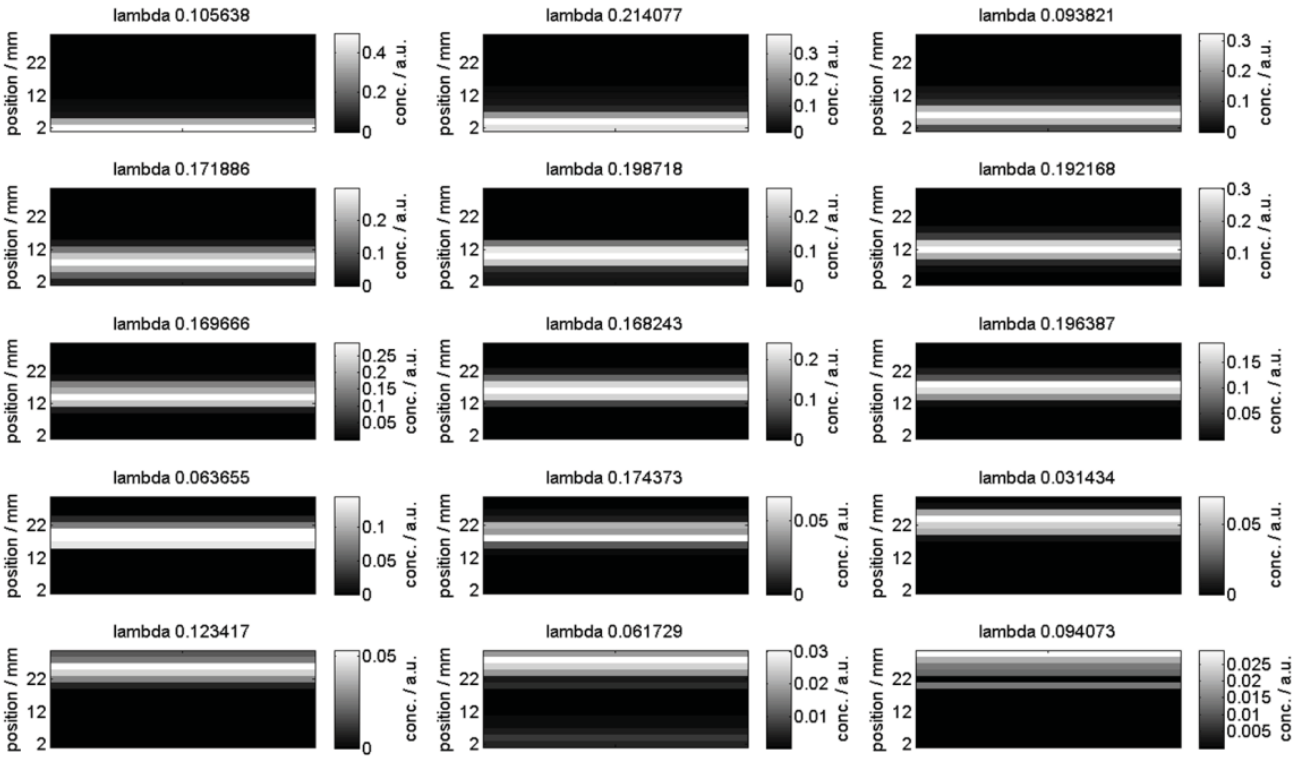

Image 6 The reconstruction results of the sample, which was used for the system matrix measurement. Lambda gives the used regularization parameter, the colour map shows the concentration and the position of the sample in mm is spared on the ordinate. The sample point is spread over the whole abscissa. In each picture the scanner is positioned at the bottom.

5 Acknowledgment

This project has been supported by the German Federal Ministry of Education and Research (BMBF Grant Number 01EZ0912).

6 References

[1] T. M. Buzug, G. Bringout, M. Erbe, K. Gräfe, M. Graeser, M. Grüttner, A. Halkola, T. F. Sattel, W. Tenner, H. Wojtczyk, J. Hägele, F. M. Vogt, J. Barkhausen, K. Lüdtke-Buzug: Magnetic Particle Imaging: Introduction to Imaging and Hardware Realization, Zeitschrift für Medizinische Physik, vol. 22, no. 4, pp. 323-334, 2012

[2] B. Gleich, J. Weizenecker: Tomographic imaging using the nonlinear response of magnetic particles, Nature, vol. 435, pp. 1214-1217, 2005

[3] T. Wawrzik, F. Ludwig, M. Schilling: Two-dimensional magnetic particle imaging, Magnetic Nanoarticles-Particle Science, Imaging Technology, and Clinical Applications, Proceedings of the First International Workshop on Magnetic Particle Imaging, World Scientific, Buzug et al., vol. 1, pp. 100-105, Singapore 2010

[4] P. Vogel, M. A. Rückert, P. Klauer, W. H. Kullmann, P. M. Jakob, V. C. Behr: Slicing Frequency Mixed Traveling Wave for 3D Magnetic Particle Imaging, Magnetic Particle Imaging, SPPHY, vol. 140, pp. 231-235, 2012

[5] P. W. Goodwill, G. C. Scott, P. P. Stang, S. M. Conolly: Narrowband Magnetic Particle Imaging, IEEE Transactions on Medical Imaging, vol. 28, pp. 1231-1237, 2009

[6] T. F. Sattel, T. Knopp, S. Biederer, B. Gleich, J. Weizenecker, J. Borgert, T. M. Buzug: Single-sided device for magnetic particle imaging, Journal of Physics D: Applied Physics, vol. 42, no. 2, pp. 1-5, 2009

[7] B. Ruhland, K. Baumann, T. Knopp, T. F. Sattel, S. Biederer, K. Lüdtke-Buzug, T. M. Buzug, K. Diedrich, D. Finas: Magnetic particle Imaging durch superparamagnetische Nanopartikel zur Sentinellymphknotendetektion beim Mammakarzinom, Geburtshilfe und Frauenheilkunde, vol. 69, pp. 758, 2009

[8] T. Knopp, J. Rahmer, T. F. Sattel, J. Weizenecker, B. Gleich, J. Borgert, T. M. Buzug: Weighted iterative reconstruction for magnetic particle imaging, Physics in Medicine and Biology, vol. 55, pp. 1577-1589, 2010

[9] S. Kaczmarz: Angenäherte Auflösung von Systemen linearer Gleichungen, Bull. Internat. Acad. Polon. Sci. Lett., A35:355-357, 1937

[10] J. Weizenecker, J. Borgert, B. Gleich: A simulation study on the resolution and sensitivity of magnetic particle imaging, Phys. Med .Biol., vol. 52, pp. 6363-6374, 2007

Spectral editing at 7 T: In vivo GABA separation in mouse brain

Niebergall, Aaron[1,2], Moussavi, Amir[2], Baudewig, Jürgen[2], and Boretius, Susann[2]
[1]Institut für Medizintechnik, Universität zu Lübeck, Lübeck, Deutschland
[2]Sektion Biomedizinische Bilgebung, Klinik für Radiologie und Neuroradiologie, UKSH, Kiel, Deutschland

Abstract

Magnetic-resonance-spectroscopy is a non-invasive technique that permits to measure metabolic changes in brain tissue. Purpose of this work was the implementation of a Jdifference technique for GABA separation in mice on a 7 T animal MR system. The editing technique was realized using a MEGA-PRESS scheme. First in vitro experiments were carried out to validate the functionality. Second in vivo experiments (10 mice) were performed to verify the separation of GABA in tiny brain regions in living mice. The separation by frequency selective editing was possible but only in 3 of 10 mice a reliable quantification could be realized. The direct quantification by linear combination of models spectra and a standard PRESS spectra at ultra high field MRS is superior to the spectral editing method in living mice. In order to reveal reliable GABA estimates at small voxel sizes in vivo further adaptations are necessary.

1 Introduction

Being truly noninvasive, localized proton magnetic resonance spectroscopy (MRS) can provide insights into the chemical composition and metabolism of intact living organism. It has been successfully applied in biomedical research and clinical diagnostics. The number of substances detectable by MRS strongly depends on the spectral resolution. At ultra high magnetic field, MRS benefits from both the increased signal to noise ratio and the improved spectral resolution due to the increased chemical shift dispersion. For the separation of metabolite likewise important is a narrow line width. The line width, however, strongly depends on the homogeneity of the magnetic field which is on the other hand more difficult to achieve at higher magnetic field strength. One metabolite of great interest, particular in neuroscience, is the inhibitory neurotransmitter γ-aminobutyric acid (GABA). Alteration of GABA concentration has been reported for a variety of neurological diseases [1]. However, compared to other brain metabolites, the in vivo detection of GABA is hampered by its low concentration of about 2 mM and an overlap of all its resonances with other resonances of higher amplitudes such as creatine (Cr), glutamate (Glu) and N-acetylaspartate (NAA). GABA (NH-$^{\alpha}CH_2$-$^{\beta}CH_2$-$^{\gamma}CH_2$-COOH) has six protons in the three methylene groups which are detectable by MRS: The triplet resonances of $^{\alpha}H$ and $^{\gamma}H$ appear at 2.28 ppm and 3.01 ppm, respectively, and the quintet $^{\beta}H$ at 1.89 ppm. The metabolite resonances are commonly expressed as a frequencyoffset to a reference substance, here tetramethylsilane (TMS). Instead of giving the frequency offset in Hertz, the field strength independent unit parts per million (ppm) is commonly used, which is related to the larmor precession frequency of the ^1H protons, ν_0 as follows:

$$1\ ppm = \nu_0 \cdot 10^{-6}.$$

The possibility of in vivo quantification of GABA has been demonstrated in experimental studies in animals using ultra high field systems (>7 T) under very good shim conditions [2]. Most of the clinical studies, however, operate at 1.5 T and 3 T MR-systems. At this field strength a direct separation of the GABA peaks is not possible because of the low spectral resolution. The most common method to enable GABA quantification at low-field systems is the so called frequency selective spectral editing [3], that was successfully applied to other metabolites like lactate as well [4]. This method utilizes the scalar coupling or J-coupling of spins. Scalar coupling is caused by electrons in chemical bonds between nuclei with magnetic moments leading to a splitting of resonances into multiplets depending on the number of interacting chemical bonds. The amount of resulting the chemical shift of the resonance splitting refers to the coupling constant J which is stated in hertz and independent of the field strength. For example, if there are two coupled spins with different resonance frequencies the singlet resonance peak of each spin is split up into two peaks with a frequency shift depends on the scalar coupling constant. This simple example is illustrated in Image 1. The resulting frequency shift leads to a phase difference of the two spin populations as a function of echo time called scalar coupling evolution. In the case of GABA, for both pairs $^{\gamma}H$ and $^{\beta}H$, and $^{\gamma}H$ and $^{\alpha}H$ J_{GABA} is 7.3 Hz. To separate coupled from uncoupled spins, like the protons of creatine resonating at 3.03 ppm and the H of GABA, frequency selective 180° pulses can be applied to reverse the echo-time-depending phase shift of the GABA triplet. While spectra of coupled spins appear different with and without these frequency selective pulses, theoretically no differences will be observed for uncoupled spins. This fact is utilized in the MEGA (MEschner-GArwood)[5] approach that combines frequency selective 180° pulses with basic sequences for localized MRS, as PRESS (point resolved spectroscopy)[6]

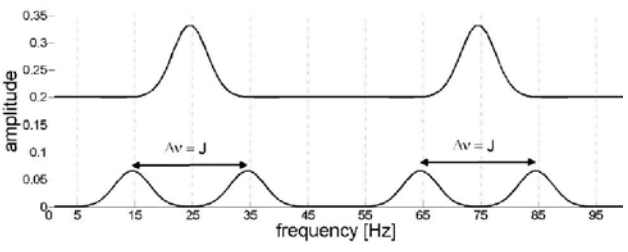

Image 1: Example of coupling scheme of two spins at different center frequencies ν_1 = 25 Hz and ν_2 = 75 Hz and the coupling constant J.

and STEAM (stimulated echo acquisition mode)[7]. There are several human studies at 3 T e.g. [8], which describe optimized editing versions for suppressing co-edited macromolecules. The increasing number of available ultra high field human MR-systems has resulted in first promising applications of this technique at 7 T e.g. [9]. Only little is known about the possible benefit of this technique in small animal research. Particular in relation to translational research and the increasing number of mouse models being available, however, this is of high interest. The goals of this study were (1) to implement a J-difference GABA editing technique at a 7 T animal MR system, (2) to evaluate its efficiency and the accuracy of GABA quantification in vitro, and (3) to explore possible benefits for its application in mice in a first in vivo study.

2 Materials and Methods

All experiments were performed at a 7 T 30 cm-bore animal MR system (Clinscan, Bruker BioSpin, Ettlingen, Germany) equipped with a BGA12S gradient system (Bruker BioSpin, Ettlingen, Germany) providing a maximum gradient strength of 660 mTm^{-1} and maximum slew rate of 4570 $Tm^{-1}s^{-1}$.The ^1H Proton resonance frequency ν_0 at 7 T is approximately 300.4 MHz. For phantom experiments a birdcage coil (inner diameter 35 mm) was used in transmit-receive mode. Mouse data was acquired with a 4-channel phased array surface coil and a birdcage coil (inner diameter 70 mm) for excitation. MEGA-PRESS is a difference method that requires at least two experiments, one with a frequency selective pulse at the resonance frequency of the metabolite, called 'ON' and another one with a pulse at an arbitrary center frequency called 'OFF'. The difference of both is the metabolite specific edited spectrum. Therefore the MEGA module was incorporated in a standard Siemens PRESS product sequence by including the following modification: We used two single-banded Gaussianshaped RF pulses with a duration of τ_{edt} = 14 ms, flip angle α_{edt} = 180° and a bandwidth of 31.52 Hz corresponding to 0.105 ppm and a combination of six spoiler gradients with an amplitude of 300 mTm^{-1}, duration of 250 µs and slew rate of

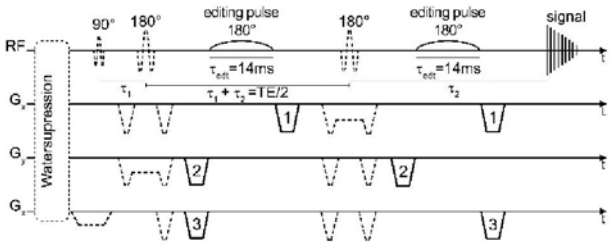

Image 2: Schematic diagram of a PRESS sequence (dashed) with single voxel excitation by a 90° pulse and two 180° slice selective refocusing pulses. Incorporated MEGA editing module (solid), (1)-(3) tag editing spoiler gradients.

60 $Tm^{-1}s^{-1}$. A standard Siemens water suppression method Water suppression Enhanced through T1 effects (WET) was taken from the PRESS product sequence with a bandwidth of 200 Hz. Position of pulses and spoiler gradients are represented schematically in Image 2, the latter are needed to crush the refocused spins of the frequency selective pulse [5]. The editing pulses (ON, OFF) were placed symmetrically around the water resonance at 4.7 ppm. To selectively invert $^{\gamma}H$ (ON experiment), the corresponding RF pulses were applied at 1.9 ppm. In the unedited case (OFF-experiment), a frequency of 7.5 ppm was chosen. The frequency shift for the editing pulses was kept variable and can be changed for other metabolites. For proper positioning of volumes-of-interest (VOI) T2-weighted images (2D FSE, TR 4000 ms, TE 50 ms, FOV 25×25 mm^2, resolution 0.1×0.1×0.4 mm^3, 40 slices) were obtained in 3 orthogonal orientations. Shimming was carried out by an advanced automatic shimming routine based on a 3D-field map provided by the manufacturer. In rare cases a manual shim correction had to be done to achieve a suitable line width of 5 to 6 Hz in phantom and 15 to 20 Hz in mouse experiments. Based on the scalar coupling constant J_{GABA} the echo time (TE) was kept constant for all experiments excepted the T2 estimation to 68 ms, due to $1/2J_{GABA}$ = TE. To avoid T1-weighting the repetition time was set to 6000 ms. 2048 data points were acquired with a bandwidth of 4900 Hz, total acquisition time (TA) differed in phantom and mouse data depending on the numbers of averages (NA). An automatic RF phase cycling was activated (16 cycle steps at two repetitions) to avoid unwanted coherences.

2.1 Phantom experiements

The phantom experiments were designed to validate and to optimize the sequence implementation. Two 15 ml phantoms (standard plastic tubes, CELLSTAR, Greiner bio-one, Frickenhausen) were used, one with a solution of 100 mM GABA in water, pH 7.2, (GABA, Sigma, Deisenhofen) and another with a mixture of the relevant, the GABA quantification possibly confounding metabolites (50 mM GABA, 50 mM Glu, 100 mM NAA and 100 mM Cr). Caustic soda (NaOH) and hydrochloric acid (HCl) were used to adjust the solutions to a pH-value of 7.2. The cubic VOIpha (3×3×3 mm^3 = 0.027 ml) was placed at the isocenter of the magnet for best field homogeneity and shimming performance. Phantom data was averaged over 32 or 64 repetitions to increase the signal-noiseratio (SNR), resulting in an acquisition time of 3:36 min or 6:24 min for a single spectrum. To calculate the T2 relaxation time and to verify the editing efficiency ON-spectra were acquired at 12 different echo times (68–289 ms). Then the spectrum was phased by an in-house routine based on the resonance of 3.01 ppm. The signal intensity is estimated by the integral of the $^{\gamma}CH_2$ peak.

2.2 Animal experiements

All mouse experiments were performed in accordance with German animal protection laws after approval by the responsible governmental authority. Adult mice (n = 10) were initially anesthetized with 5% isoflurane, subsequently intubated, positioned on a home-built animal bed and kept under anesthesia with 1.75% isoflurane in ambient air plus oxygen. Body temperature was kept constant at 36.0±0.5 °C. Spectra (ON, OFF) from two VOI were acquired: one (VOI_{small}: 1.0×3.9×3.2 mm^3 = 12.48 µl, NA=

128, TA= 13:12 min) placed at the mouse cortex and a larger one (VOI_{large}: 4.0×3.0×4.0 mm^3 = 48 µl, NA= 128, TA= 13:12 min) in the middle of the mouse brain, covering the major parts of the cortex, the lateral ventricles and the striatum. For comparison conventional PRESS spectra (TR 6000 ms, TE 10 ms, NA= 64, TA= 6:24 min) were obtained from the same location of the brain. Mouse data was analyzed using a GABA-MRS analysis Tool (Gannet 2.0 beta, [10]) and the "*linear combination of model in vitro spectra*" (LCModel, LCMODEL Inc., Oakville, Ontario, Canada). The latter was used to analyze the spectra acquired by the conventional PRESS sequence. The proceeding pipeline of Gannet includes preprocessing steps: exponential line broadening, frequency and phase correction, outlier rejection and subtraction of the spectra; the fitting routine includes a nonlinear least-squares method. The fits are achieved by a single gaussian peak for GABA, a gaussianlorentzian model for water and a single lorentzian peak for creatine. The integral of each fit is used for quantification.

3 Results and Discussion

3.1 Phantom experiments

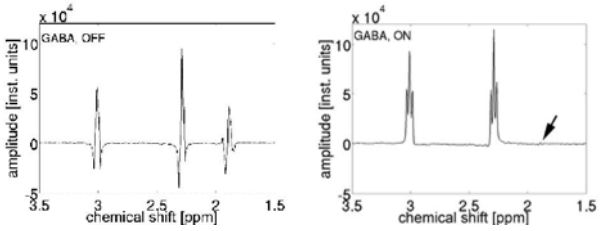

Image 3: *In vitro* experiments of a pure GABA solution. Left: unedited spectrum (OFF). Right: edited spectrum (ON)

OFF- (7.5 ppm, Image 3, left) and ON- (1.9 ppm, Image 3, right) spectra of a pure GABA solution showed the expected behavior of coupled spin systems. Main influences of the frequency selective pulses at 1.9 ppm ($^{\beta}CH2$) are shown in Image 3, right. The outer resonance lines at about 3.01 ppm ($^{\gamma}CH2$) and 2.28 ppm ($^{\alpha}CH2$) are fold up due to the reversal of the echo-time- dependent phase shift caused by frequency selective pulses at 1.9 ppm, which in addition suppressed the GABA resonance at this frequency (arrow in Image 3, right). The OFF-spectrum of the mixed solution (Image 4, middle) demonstrates the strong overlap of the GABA resonance at 3.01 ppm with that of creatine at 3.03 ppm. However, by subtracting the OFF from the ON spectrum, the GABA peak becomes clearly visible (Image 4, bottom). Therefore the phantom data clearly demonstrated that the editing pulses worked as expected and that the separation of GABA and creatine was possible with the implemented method. The huge negative peak in the difference spectrum at about 2 ppm belongs most likely to the resonance of NAA and was caused by the spectral suppression of NAA during the ON experiment because of the frequency difference of NAA and GABA (0.1 ppm/30Hz) relative to, the large bandwidth of the frequency selective pulse (0.105 ppm/31Hz).

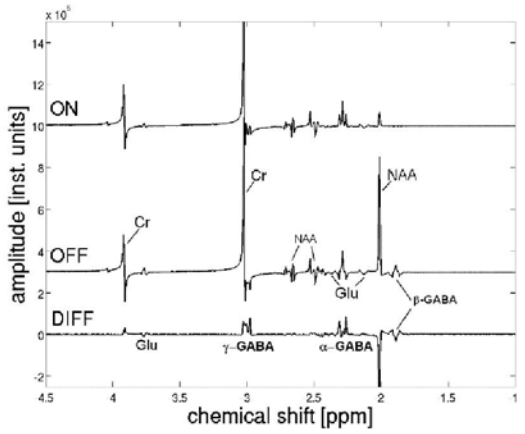

Image 4: ON spectrum (top), OFF spectrum (middle) and the difference spectrum (bottom) of the mixed phantom, including relevant metabolites of the animals metabolism like Cr, NAA, Glu and GABA.

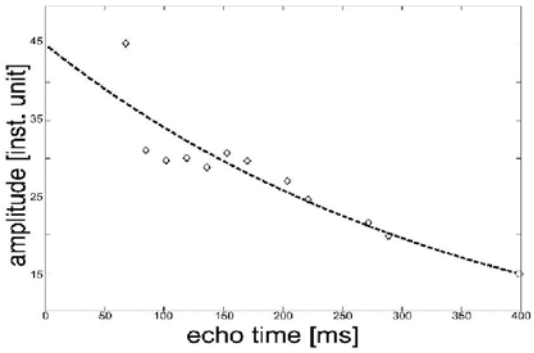

Image 5: ON spectra recorded at different echo times (TE = 68-289 ms) to estimate the $T2_{phantom}$ of a GABA solution *in vitro*.

Consequently, using short pulse duration, coediting is unpreventable. Since pulse duration and bandwidth are directly connected to one another which is expressed in a constant bandwidth-timeproduct. Thus to realize a sharper frequency selective pulse its length has to be increased. If we want to keep the echo time as short as possible (e.g. 68 ms), the applied crusher gradients have to be adapted. With shortest possible duration and higher amplitudes of the spoiler gradients in the MEGA module a pulse duration of 19 ms could be achieved. Another possibility to sharpen the RF pulse is to accept a longer echo time [8] and the resulting reduction in signal to noise ratio. A feature provided by MEGA-PRESS is the estimation of the substance-specific T2 relaxation time. Therefore an exponential fit (CurveFitting Toolbox, Matlab, Mathworks, Natick, USA) was produced based on the integral of the signal intensity, revealing an in vitro T2 relaxation time of GABA of 390 ms (Image 5), which poorly matches with the results of a previous study (T2 = 204 ms) [8]. One reason for this discrepancy of our T2 estimation of GABA to other studies may be the missing of data points at short echo times. The shortest echo time which could be realized was 58 ms, because of the additional editing RF pulses and gradients, so this method may be more appropriate for samples with long T2.

2.2 Animal experiements

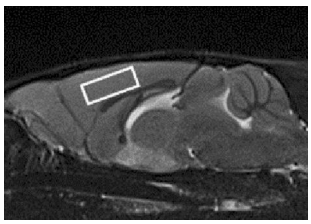

(a) VOI_{small} position in the cortex of a mouse for in vivo experiment.

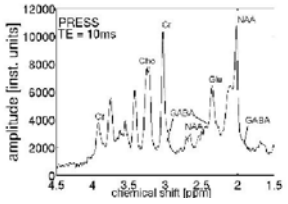

(b) PRESS spectrum for LCModel analysis.

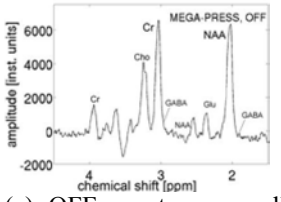

(c) OFF spectrum, small VOI

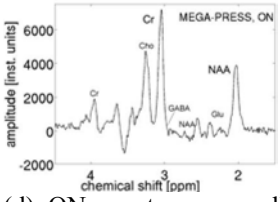

(d) ON spectrum, scmall VOI

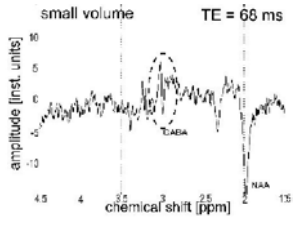

(e) Difference spectrum, small VOI

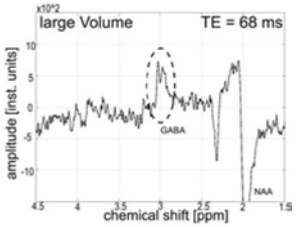

(f) Difference spectrum, large VOI

Image 6: Results of the in vivo experiments.

Preliminary in vivo data is shown in Image 6. Compared to the conventional PRESS spectrum obtained with an echo time of 10 ms (Image 6b), the OFF-spectrum (TE = 68 ms) revealed a signal drop for almost all metabolites, which could be mainly explained by signal attenuation due to T2 relaxation. Comparison of the signal intensity at equal echo times (data not shown), however, still revealed a higher SNR in PRESS spectra compared to those obtained by MEGA-PRESS. Possible reasons, that have to be clarified in subsequent experiments, are, for example, effects of diffusion weighting by additional crusher gradients, imperfect spectral editing and RF pulses, unwanted coherences and unfavorable combination of single spectra. Although OFF- (Image 6c) and ON- (Image 6d) spectra of the small VOI located in the cortex allowed for a clear peak detection, the corresponding difference spectra, however, were very noisy. Accordant, an appropriate curve fitting of the expected GABA peak at 3.01 ppm and due to that a quantification was only possible in 3 of 10 mice. In contrast to that, analyses of the conventional PRESS spectra (Image 6b) using LCModel reproducibly revealed a GABA concentration of 2.3±0.3 mM in this group of mice. Improvement of SNR by a factor of 2 due to an increase in voxel size dramatically improved the detectability of GABA in the resulting difference spectrum (Image 6f). Unfortunately the large voxel size of 4.0×3.0×4.0 mm^3 makes exclusive neurochemical analyses of tiny brain regions like the hippocampus in mice impossible. Under the condition of narrow line widths the direct detection of GABA by linear combination of model in vitro spectra seems to be superior to the difference approach used in the implemented spectral editing method. In other words: the latter needs to be further adapted to the requirements of higher field (e.g. partial reduction of TE, use of additional resonances) and the small size of mouse brain (e.g. longer measurement time, use of adapted coils for signal detection, alternating acquisition of ON and OFF spectra). However, this finding may look completely different in regions with strong field inhomogeneity and broadening of the line width such as regions close to the auditory canal and necrotic tumors.

4 Conclusion

A MEGA-PRESS sequence that allows *J*-difference editing has been successfully implemented on a 7 T small animal MR-system. *In vitro* measurements using phantoms with solutions of the relevant substances confirmed the functionality of the implemented sequence. Moreover, *in vivo* experiments demonstrated the feasibility of GABA separation by spectral editing in living mice. However, to fulfill current requirements of brain research in mice, further adaptations are necessary to enable a sufficiently small voxel size within a measurement time feasible for *in vivo* experiments under anesthesia.

5 References

[1] C. Smith-Hicks, "GABAergic dysfunction in pediatric neurodevelopmental disorders," Frontiers in Cellular Neuroscience, vol.7, no. 269, 2013

[2] I. Tkac et al., "Highly resolved in vivo 1H NMR spectroscopy of the mouse brain at 9.4 T," Magnetic Resonance in Medicine, vol. 52, no. 3, pp. 478–484, 2004

[3] R. L. Rothman, O. A. Petroff, K. L. Behar, and R. H. Mattson, "Localized 1H nmr measurements of -aminobutyric acid in human brain in vivo," Proceedings of the National Academy of Sciences of the United States of America, vol. 90, no. 12, pp. 5662–5666, 1993

[4] J. Star-Lack, et al. "In vivo lactate editing with simultaneous detection of choline, creatine, naa, and lipid singlets at 1.5T using PRESS excitation with applications to the study of brain and head and neck tumors," Journal of Magnetic Resonance, vol. 133, no. 2, pp. 243–254, 1998

[5] M. Mescher, H. Merkle, J. Kirsch, M. Garwood, and R. Gruetter,"Simultaneous in vivo spectral editing and water suppression," NMR in Biomedicine, vol. 11, no. 6, pp. 266–272, 1998

[6] R. Ordidge, M. Bendall, R. Gordon, and A. Connelly, "Volume selection for in-vivo biological spectroscopy," Magnetic Resonance in Biology and Medicine, p. 387, 1985

[7] J. Frahm, et al., "Localized high-resolution proton NMR spectroscopy using stimulated echoes: Initial applications to human brain in vivo," Magnetic Resonance in Medicine, vol. 9, no. 1, pp. 79–93, 1989

[8] R. Edden, N. Puts, and P. Baker, "Macromolecule-suppressed GABA edited magnetic resonance spectroscopy at 3T," Magnetic Resonance in Medicine, vol. 68, no. 3, pp. 657–661, 2013

[9] I. Tkac et al., "In vivo 1H NMR spectroscopy of the human brain at 7T," Magnetic Resonance in Medicine, vol. 46, no. 3, pp. 451–456, 2001

[10] R. Edden, N. Puts, A. Harris, P. Barker, and C. Evans, "Gannet: A batchprocessing tool for the quantitative analysis of gamma-aminobutyric acid edited mr spectroscopy spectra," Journal of Magnetic Resonance Imaging, to be published, 2013

A robust and compact representation for magnetic fields in magnetic particle imaging

G. Bringout[1] and T. M. Buzug[1]

[1]Institute of Medical Engineering, Universität zu Lübeck, Lübeck, Germany, {bringout,buzug}@imt.uni-luebeck.de

Abstract

In this contribution, a simple representation for magnetic fields based on spherical harmonics is presented. Compared to the acquisition on a Cartesian grid, it reduces the amount of acquired and stored data, and may increase the precision of the field representation in given scenario. The series expansion of the field generated by a drive coil is presented and the truncation error is studied. Furthermore, time and space models of the magnetic fields generated by a field-free point and a field-free line scanner using the spherical harmonic representation are presented. The proposed representation has the potential to improve the analysis of the MPI technology, by providing a compact and flexible way to represent MPI scanners and the associated magnetic fields.

1 Introduction

To date, magnetic fields used in magnetic particle imaging (MPI) scanners have mostly been defined implicitly by the coils needed to generate them or by an ideal approximation of their topology [1].

As many aspects linked to the MPI technology need to simulate, evaluate and validate the exact topology of magnetic fields, a better way to represent the fields is required. This may aim to a broader definition of the signal generation in scanners, analytical ways to design scanners, better accuracy of modeled system matrices, faster reconstruction for field-free line scanners or a technique for the quality control during the production of scanners.

An appropriate way to represent the magnetic field on a 2D- or 3D-Cartesian grid is to fit some polynomials in specific points on the grid in order to approximate the field topology. However, this technique includes two major drawbacks. First, the number of measured points may increase with the surface, volume or resolution increase, leading to a huge amount of data, which may be difficult to store and work with. Second, the approximation of the field topology with polynomials may include large errors due to an insufficient sampling and the use of fitting models with limited order [2].

The representation of divergence-free fields using series expansion overcomes those two limitations. For most coils in MPI, as the length to diameter ratio is below ten, the spherical harmonics series expansion (SHSE) is preferred. Indeed, the effects of the coil's end parts may still have a huge influence on the magnetic field topology in the center of it, and a spherical representation is better suited for this situation [2].

However, the SHSE is not exempt from drawbacks, one of them being the interpretation errors caused by the use of different normalizations. Nevertheless, this may also be advantageously used, as the different normalization may facilitate the direct evaluation of derived quantities. For example, with the Schmidt quasi-normalization, each coefficient represents the maximum amplitude reached by the corresponding spherical harmonic on a sphere, which helps to quickly evaluate the field amplitude at different position.

In this contribution, a wide spectrum of the tools needed to understand and use this representation are presented. The SHSE is depicted in different ways, so that a correlation between the SHSE and other ways of representing magnetic fields can easily be made. To highlight the differences between the SHSE and the Cartesian representation, the magnetic field generated by a drive coil is taken as an example. Finally, theoretical field-free point (FFP) and field-free line (FFL) scanners are presented, to demonstrate the compactness and flexibility of this representation.

2 Methods

In this section the basic mathematical principles of the SHSE and its applications to the magnetic field measurement is presented.

2.1 Basic differential equation

In an investigated area, where no electric current flows, every component of a magnetic field $B_i, i = x, y, z$ satisfies the Laplace equation

$$\Delta B_i = 0 \tag{1}$$

due to Maxwell's equations [3]. To solve the Laplace equation for a given problem, some constraints have to be imposed. In the case of solving the problem with the SHSE, the Dirichlet boundary condition

$$\begin{cases} \Delta B_i = 0 & \text{, in } \{\mathbf{x} \in \mathbb{R}^3, \|\mathbf{x}\| < R\} \\ B_i(\mathbf{x}) = g(\mathbf{x}) & \text{, in } S_R^2 \end{cases} \tag{2}$$

is used. Here the values of the magnetic field components have to be known on the sphere S_R^2 with fixed radius R and are described by a continuous function g.

2.2 Solution

Applying spherical coordinates (r, θ, φ), the solution of the problem (2) is given by the series expansion

$$B_i(r,\theta,\varphi) = \sum_{l=0}^{\infty} \sum_{m=-l}^{l} c_{lm}^R \left(\frac{r}{R}\right)^l Y_{lm}(\theta,\varphi), \qquad (3)$$

with coefficients c_{lm}^R of the normed real spherical harmonics Y_{lm} [4]. The spherical harmonics, shown on Fig. 1, are defined by

$$Y_{lm}(\theta,\varphi) = \begin{cases} \sqrt{2} K_l^m \cos(m\varphi) P_l^m(\cos\theta) & , m > 0 \\ K_l^0 P_l^0(\cos\theta) & , m = 0 \\ \sqrt{2} K_l^{|m|} \sin(|m|\varphi) P_l^{|m|}(\cos\theta) & , m < 0 \end{cases} \qquad (4)$$

with P_l^m the associated Legendre polynomials and K_l^m the normalizing factor defined by

$$K_l^m = \sqrt{\frac{(2l+1)}{4\pi} \frac{(l-m)!}{(l+m)!}}. \qquad (5)$$

Here $l = 0, 1, 2, ...$ denotes the degree and m the order of the spherical harmonic, with $-l \leq m \leq l$. The associated Legendre polynomials can be calculated using the recursion

$$\begin{aligned} P_0^0(x) &= 1 \\ P_m^m(x) &= (2m-1)!!(1-x^2)^{\frac{m}{2}} \\ P_{m+1}^m(x) &= x(2m+1)P_m^m \\ P_l^m(x) &= x\frac{2l-1}{l-m}P_{l-1}^m(x) - \frac{l+m+1}{l-m}P_{l-2}^m(x) \end{aligned} \qquad (6)$$

with $0 \leq m \leq l$ and the double factorial $(2m-1)!! = \prod_{i=1}^{m}(2i-1)$.

2.3 Projection formula

The normalization presented in (5) forms an orthonormal basis of the square-integrable functions of the unit sphere S^2 with respect to the standard scalar product

$$\begin{aligned} \langle f, g \rangle &= \int_{S^2} f g \, \mathrm{d}\Omega \\ &= \int_0^{2\pi} \int_0^{\pi} f(\theta,\varphi) g(\theta,\varphi) \sin(\theta) \, \mathrm{d}\theta \, \mathrm{d}\varphi. \end{aligned} \qquad (7)$$

Thus, the coefficients c_{lm}^R from (3) can be calculated by the projection formula

$$c_{lm}^R = \int_0^{2\pi} \int_0^{\pi} g(\theta,\varphi) \, Y_{lm}(\theta,\varphi) \sin(\theta) \, \mathrm{d}\theta \, \mathrm{d}\varphi. \qquad (8)$$

Thereby, it is sufficient to know the magnetic field on a sphere to determine the coefficients which describe the entire magnetic field of the whole ball.

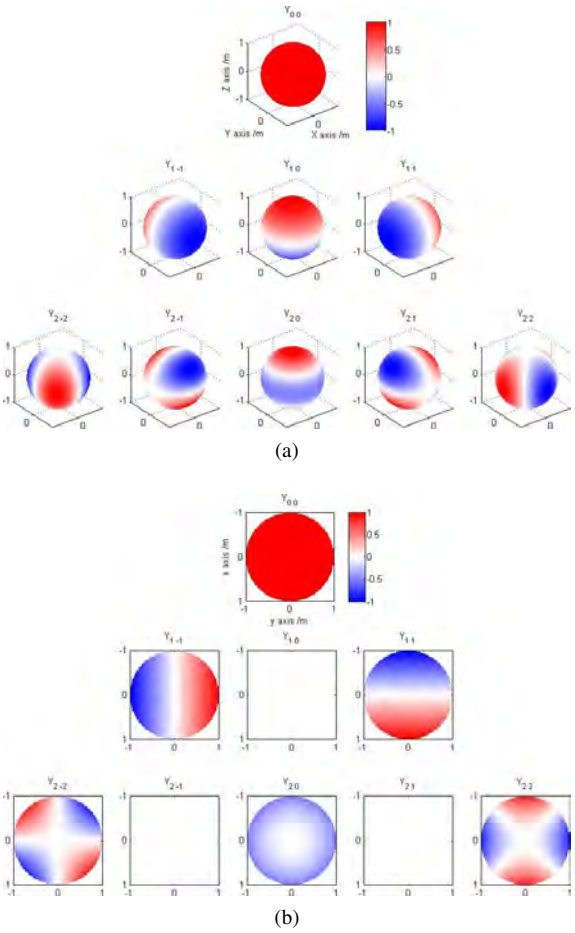

Figure 1: Two ways to represent the spherical harmonics Y_{lm} with $l \leq 2$ and $-l \leq m \leq l$. θ and φ are interpreted as spherical coordinates of the unit sphere. (a) The amplitude is represented as color variation. (b) The amplitude on the xy-plane is represented as color variation.

2.4 Normalization

Several types of normalization are commonly used, based on the wanted properties of interest. Outside the mathematical normalization presented in (5), the Schmidt quasi-normalization can also be used. It is defined as

$$K_l^m = \sqrt{\frac{(l-m)!}{(l+m)!}}, \qquad (9)$$

which normalize the maximum of the spherical harmonics to one [5]. Therewith, the coefficients of the SHSE correlate immediately to the maximum influence of the corresponding spherical harmonics. However, this normalization provides no orthonormal basis and thus the projection formula (8) has to be adapted by dividing through the squared norm of the the quasi-Schmidt normalized spherical harmonic:

$$\|Y_{lm}\|^2 = \frac{4\pi}{2l+1}. \qquad (10)$$

2.5 Numerical integration

A simple way to evaluate the magnetic field on a sphere is to measure its amplitude at some discrete points. In order

to do this, the integral of the projection formula (8) has to be replaced by a numerical integration formula

$$\sum_{i=1}^{N_\theta}\sum_{j=1}^{N_\varphi}\omega_i^\theta\,\omega_j^\varphi\,g(\theta_i,\varphi_j)\,Y_{lm}(\theta_i,\varphi_j)\sin(\theta_i) \qquad (11)$$

with N_θ discretization positions of θ, N_φ discretization positions of φ and their corresponding weights ω_i^θ and ω_i^φ. Due to the independence of φ and θ in the spherical harmonics definition (4), the integral can be split into the φ-part and the θ-part.

As the φ-part contains only cosine or sine functions, the integration in done with the left rectangle method using equidistant discretization positions $\varphi_j = (j-1)\frac{\pi}{N_\varphi}$ and the weights $\omega_j^\varphi = \frac{\pi}{N_\varphi}$.

In contrast to this, after the substitution of $s = \cos(\theta)$, the θ-part only contains the associated Legendre polynomials. Knowing that the Gaussian quadrature, also known as the Gauss-Legendre quadrature, uses weights and discretization positions determined using the Legendre polynomials, it is therefore optimal for integration of the θ-part. The N_θ discretization positions s_i are the zeros of the $N_{\theta^{th}}$ Legendre polynomial and the weights ω_i^θ are adapted in such a way, that with N_θ discretization positions a polynomial with degree $2N_\theta - 1$ can be exactly integrated [6]. The discretization of θ is therefore given by $\theta_i = \cos^{-1}(s_i)$.

2.6 Maximal order and degree

Assuming that the measured magnetic field can be completely described by spherical harmonics up to order $(l_{\max}, m_{\max})$, with $l_{\max}+1$ sampling points in θ-direction and $2m_{\max}+1$ sampling points in φ-direction, the coefficients can be exactly computed with the proposed numerical integration formulas. This is due to the special structure of the spherical harmonics and the properties of the used numerical integration formula.

2.7 Implementation

Calculations have been done in Matlab (Matlab 7.11.0 64bit, Mathworks, Natick, USA). The implementation is available on http://www.imt.uni-luebeck.de and http://github.com/gBringout/CoilDesign.

3 Results

In this section, practical examples are given to emphasize the advantages and limitations of the SHSE for the MPI community.

3.1 Truncation error

It has been seen that a magnetic field containing a finite sum of spherical harmonics can be represented by its value on a finite number of points. But, for a given coil, it is hard to know, which spherical harmonics are included in the generated magnetic fields. Thus, it is likely that truncation errors will happen when choosing a maximal order and degree for the representation.

Table 1: Truncation error evaluation for a drive coil.

# of points	$(l_{\max}, m_{\max})$	$\frac{\Delta c_{00}}{c_{00}^{GS}}$	$\frac{\Delta c_{20}}{c_{20}^{GS}}$	Maximum error $\frac{\Delta c_{lm}}{c_{lm}^{GS}}$	(l,m)
45	(4,4)	0.4%	0.9%	4.6	(4,4)
66	(5,5)	0.1%	0.8%	4.3	(4,4)
6216	(55,55)	$2e^{-8}$	$6e^{-8}$	1374	(51,41)

In order to evaluate these errors, three projections of the magnetic field generated by a coil were calculated on different sets of points and compared. The coil is shown in Fig. 2a and the results are shown in Table 1. The "gold standard" coefficient c_{lm}^{GS} were approximated by a series expansion up to degree and order 120 on 29161 points. The coefficient c_{lm} were evaluated with a series expansion up to order and degree (4,4), (5,5) and (55,55) and the absolute error was calculated as $\Delta c_{lm} = c_{lm} - c_{lm}^{GS}$.

Considering the two coefficients which have the highest amplitude, namely c_{00} and c_{20} for the presented coil, a series expansion up to order and degree 4 is sufficient to keep the truncation error below 1 %. Even if the maximum error reach 460 % for the spherical harmonic of order 4 and degree 4, it has to be noted that the associated coefficient are here of small amplitudes, as shown in Fig. 2b.

3.2 Compactness of the representation

A field of degree $l_{\max} = 4$ and order $m_{\max} = 4$ requires only $(4+1)*(2*4+1) = 45$ data points per field direction to be represented. Furthermore, the storage of only 3*25 points is necessary after the usage of the projection formula (11). Those coefficient enables the reconstruction of the field anywhere in a ball of radius R with no other intrinsic resolution limitation. In comparison, a Cartesian grid as shown in Figure 2a in a 9 cm radius circle with a resolution of $2*2$ mm^2 requires data on 6361 points.

3.3 Flexibility - theoretical MPI scanner

Theoretical scanners can be described by as little as thirteen factors for the case of 3D FFP scanner and fourteen for a 2D FFL scanner.

As shown in Table 2, six different SHSE coefficients linked to four different values are enough to describe the whole field topology. To provide the time variation of the fields, three frequencies have to be applied on the corresponding coefficients, knowing that the excitation is always produced via in-phased sinusoidal signal. Thus, only $6+4+3=13$ factors are needed to fully described a theoretical 3D FFP scanner using the SHSE.

Similarly, a 2D FFL scanner is described by nine SHSE coefficients and three related values as shown in Table 3. As for FFP scanners, sinusoidal signals are used to create the signal and spatially encode it. But, when FFP scanners use simply three sinusoidal functions, FFL scanners use amplitude modulated signals for the drive fields. Those functions

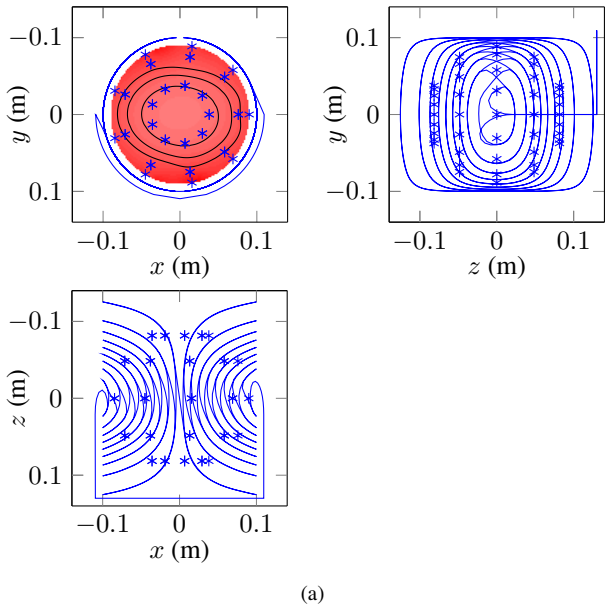

(a)

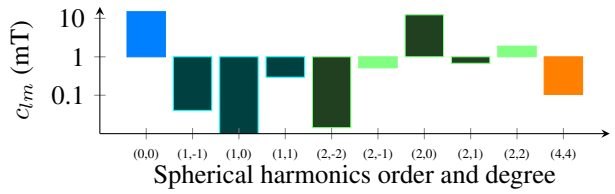

(b)

Figure 2: Representation of a drive coil with associated sampling points. (a) Front, side and top view of the model, respectively. On the front view, B_x is also represented in the xy plan. The color bar is similar to the one used in Fig 1. The contour represents the 10, 20 and 30% homogeneity limits, starting in the middle. (b) SHSE using the Schmidt quasi-normalization of the B_x fields up to the 4^{th} degree. The first bar represents the 0^{th} degree, the next three the 1^{st}, etc. As a logarithmic scale is used, the negative coefficient are represented with a darker color.

are $\cos(2\pi\, f_1\, t)$, $\sin(2\pi\, f_1\, t)$, $\cos(\pi\, f_1\, t) * \sin(2\pi\, f_2\, t)$ and $\sin(\pi\, f_1\, t) * \sin(2\pi\, f_2\, t)$ for the Quad_0, Quad_{45}, Drive X and Drive Y generators, respectively, where t represents the time. Thus, only two frequencies are used and $9{+}3{+}2 = 14$ factors are needed to completely described a theoretical FFL scanner.

4 Conclusion

The mathematical description, compactness and flexibility of the SHSE have been presented. Using this representation, the amount of acquired and stored data for the representation of magnetic fields can be greatly reduced in comparison to the acquisition on a Cartesian grid.
Most importantly, the community can benefit from a strong and compact way to represented the time and space variation of the magnetics fields in an MPI scanners. Coupled with the description of the signal generation, this opens the way of a full scanner optimization.

Table 2: Representation of a theoretical 3D FFP scanner.

Coil's name	c_{lm} B_x	B_y	B_z	Freq. (Hz)
Selection	$c_{11} = -a$	$c_{1-1} = a$	$c_{10} = 2a$	0
Drive x	$c_{00} = b$			f_1
Drive y		$c_{00} = c$		f_2
Drive z			$c_{00} = d$	f_3

Table 3: Representation of a theoretical 2D FFL scanner.

Coil's name	c_{lm} B_x	B_y	B_z	Freq. (Hz)
Selection	$c_{11} = -a$	$c_{1-1} = a$	$c_{10} = 2a$	0
Quad_0	$c_{11} = a$	$c_{1-1} = a$		f_1
Quad_{45}	$c_{1-1} = a$	$c_{11} = a$		f_1
Drive x	$c_{00} = b$			f_1, f_2
Drive y		$c_{00} = c$		f_1, f_2

5 Acknowledgement

The authors wish to thank Alexander Weber for his contribution to the method part. The authors gratefully acknowledge the support of the German Federal Ministry of Education and Research under grant number 13N11090 as well as the European Union and the State Schleswig-Holstein with the Program for the Future-Economy under grant number 122-10-004.

References

[1] T. M. Buzug *et al.*, "Magnetic particle imaging: Introduction to imaging and hardware realization," *Zeitschrift für Medizinische Physik*, vol. 22, no. 4, pp. 323 – 334, 2012.

[2] A. Wolski, "Maxwell's equations for magnets," in *Proceedings of the 2009 CAS-CERN Accelerator School: Specialised course on Magnets, Bruges, Belgium, 16-25 Jun 2009*, 2009, pp. 19–22.

[3] J. D. Jackson, *Classical electrodynamics*, 3rd ed. Wiley-VCH, 1998.

[4] G. B. Arfken and H. J. Weber, *Mathematical Methods For Physicists*, 4th ed. Academic press, 1995.

[5] D. Winch *et al.*, "Geomagnetism and schmidt quasi-normalization," *Geophysical Journal International*, vol. 160, no. 2, pp. 487–504, 2005.

[6] M. Hermann, *Numerische Mathematik*. Oldenbourg Verlag, 2006.

Design and Construction of a Toroidal Filter Coil for a Magnetic Particle Imaging Device

J. S. Stelzner*, M. Graeser*, T. M. Buzug
Institute of Medical Engineering, University of Luebeck, {stelzner, graeser, buzug}@imt.uni-luebeck.de
(* equally contributing authors)

Abstract

Magnetic Particle Imaging (MPI) is a medical imaging method that is based on the non-linear magnetization behaviour of superparamagnetic nanoparticles (SPION). Compared to other imaging technologies MPI provides high sensitivity, fine resolution and is capable of real time imaging. To acquire a suitable signal, a highly pure excitation field is essential. To guarantee the signal purity band pass filters are applied to supress distortions introduced by power aplifiers. The frequency filter performance is strongly affected by the quality factor of the implemented reactive parts. In this paper, the design process of a toroidal inductor is presented.

1 Introduction

The concept of MPI was first published in 2005 by Gleich and Weizenecker [1]. The basic principle of MPI lies in the excitation of SPIONs by a sinusoidal magnetic field. Due to the shape of a SPION's magnetization curve one acquires not only the excitation frequency, but also higher harmonics. This situation is depicted in image 1.

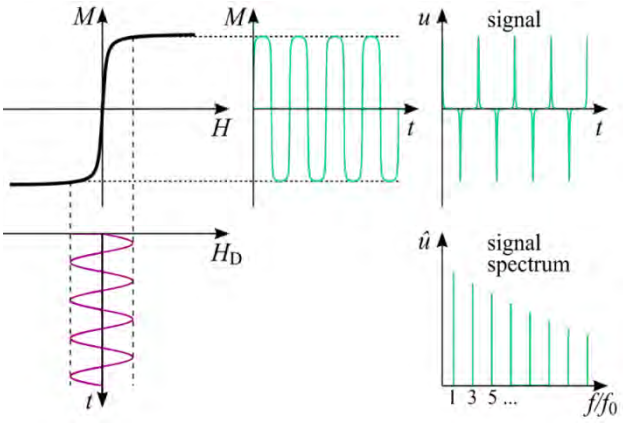

Image 1 Response of a SPION with the magnetization characteristic $M(H)$. Exciting the particle with a sinusoidal magnetic field $H_D(t)$ causes the magnetization $M(t)$, that leads to $u(t)$ with its Fourier transform $\hat{u}(f)$. [1]

One important requirement for a successful signal acquirement is the particles' property of superparamagnetism. That means that the particle state does not feature any hysteresis effects in terms of coercive fieldstrength or remanence in the absence of an external magnetic field. Another important value related to the SPIONs is the steepness of the magnetization curve, which depends among others on the diameter of the nanoparticles. When the external magnetic field H_D exceeds this value or at least transcends the linear range of the magnetization curve $M(H)$, the magnetization as a function of time $M(t)$ is no pure sinusoid. With the assistance of a receive coil setup we obtain an induced signal $u(t)$ which is proportional to the time derivative of the magnetization. Considering the Fourier transform $\hat{u}(f)$ the received signal does contain besides the excitation frequency of H_D odd multiples of this frequency. This implies the existence of SPIONs within the field of view (FOV) [2].

To gain accurate information about the amount of SPIONs within the FOV high harmonics, which are up to 10^{-6} times lower than the direct feedthrough, must be regarded. Therefore, it is indispensable to keep the excitation signal free from any higher harmonics. Distortions caused by the amplification of the signal will enter into the receive chain if they are not filtered before generating the excitation field.

After receiving the signal $u(t)$, the basic frequency has to be removed from the signal. Otherwise, the particle information would get lost due to limitation of the dynamic range in the data acquisition. This is achieved by a frequency filter as well. In this case a bandstop filter is employed.

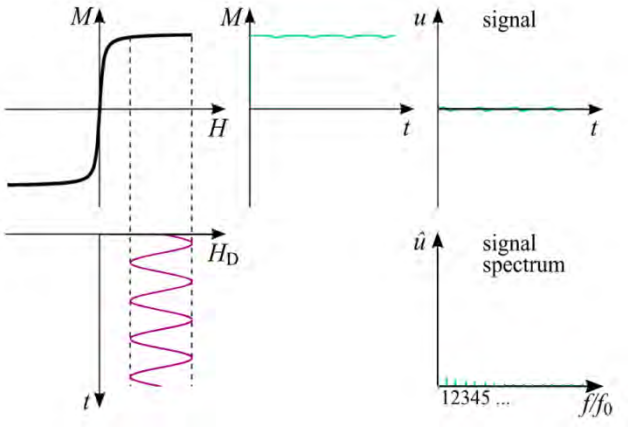

Image 2 If a constant magnetic field is superimposed to the excitation field, the working point of the magnetization is shifted into the saturation region of the SPION, so that it will not contribute to the particle signal. [1]

1.1 Spatial encoding in MPI

The selection field features a low field area and a high magnetic gradient field that drives all magnetic particles outside this low field area into magnetic saturation. This effects that only SPIOs inside the low field area contribute to the particle signal (see image 2).
There are different coil configurations and techniques to perform certain selection field techniques that feature either a field free point (FFP) [3] or a field free line (FFL) [4].

1.2 Frequency filters

Electrical frequency filters are capable of letting desired frequency ranges pass, while damping others significantly. They can be implemented with reactive elements like inductors and capacitors. With these frequency dependent impedances can be introduced in the signal chain and build a frequency dependent voltage devider. One can use such elements to perform frequency selective passing. Additionally, when we combine capacitive and inductive elements, we can create resonant circuits, which enables stopping or passing certain frequency bands exceedingly well.

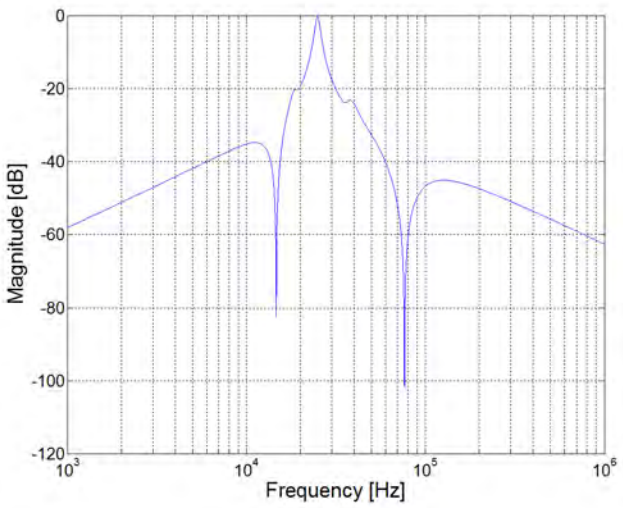

Image 3 Transfer function of a Chebyshev II bandpass filter for 25 kHz and high attenuation at 75 kHz

According to the application area as well as the impedance matching there are several methods for dimensioning the reactive components of a filtering electrical device.
In MPI, the particle signal is several orders of magnitude lower than the excitation signal, so the frequencies in the sending path which are above the excitation frequency of 25 kHz have to be attenuated as well as possible. Otherwise, the particle information,,get lost in the excitation signal harmonics. In the context of this project a Chebyshev II bandpass filter of 4th order is used. This type of frequency filter is capable of suppressing a certain frequency as illustrated in image 3. Because the magnitude of distrortion at 75 kHz (the 3rd harmonic) has the highest amplitude the parameters of the components are chosen in such a way that the attenuation at this frequency in the excitation signal is maximal.
For low attenuation in the pass band as well as high damping in the stop band, the quality factor of the reactive components has a high impact.

1.2.1 Inductive components

When the quality factor of the filter components is taken into account, the most significant aspect is the ohmic resistance of the filter coils. Another important issue is their magnetic field expansion. In contrast to field coils, the filter coil field expansion is rather an unwanted side effect, because it entails sensitivity to the surrounding. Therefore, toroidal inductors are used in the frequency filter. The field distribution of toroid coils confines itself almost entirely to the inside of the coil.
To accomplish a preferably high quality factor P.N. Murgatroyd presented a numerical procedure to calculate the optimal cross section shape of an air-cored toroidal coil according maximum inductance for a given outer radius [5].

2 Methods

The manufacturing of the toroidal coil follows in five steps. First the desired values for the inductor are determined following the Chebyshev II parameters. Then the optimal shape of the cross section, respectively its contour, is calculated by MATLAB following P.N. Murgatroyd's algorithm. Next this contour is used to create a 3D CAD model. Then the created CAD model of the torus is printed by a 3D Printer. In the end, a litz wire is wound around the torus shape and the setup is measured.

2.1 Minimum inductance determination

In order to determine parameters for the reactive elements, the program *Filter Free* by *Nuhertz Technologies* [6] was used. Because a high cancellation of the first odd harmonic at 75 kHz is desired, which can be performed by a Chebyshev II bandpass filter, this type of frequency filter will be implemented. The effective resistance is an unpreferred element, so it has to be minimized. The calculations return an inductance of 95.32 µH for the the first filter coil of the transmit filter. Calculations reveal, that a higher attenuation at 75 kHz can be achieved with a higher inductance, so the above mensioned value is a minimum value for the coil to be implemented.

2.2 Optimum shape calculation

The function, that calculates the optimal shape for the coil by means of the above mensioned algorithm was created and extendend in MATLAB.
The input parameters of this function are amongst others the frequency f for the calculation of AC losses, the outer radius $R2$, the ratio between outer and innermost diameter α_i and the relevant litz wire parameters.

After executing the related script the function returns the inductance L, the ohmic resistance R, the quality factor Q, the wire length per winding l_1 and the DC- and AC dissipation Power W_{DC} and W_{AC}. Additionally, the optimized shape is stored in the workspace.

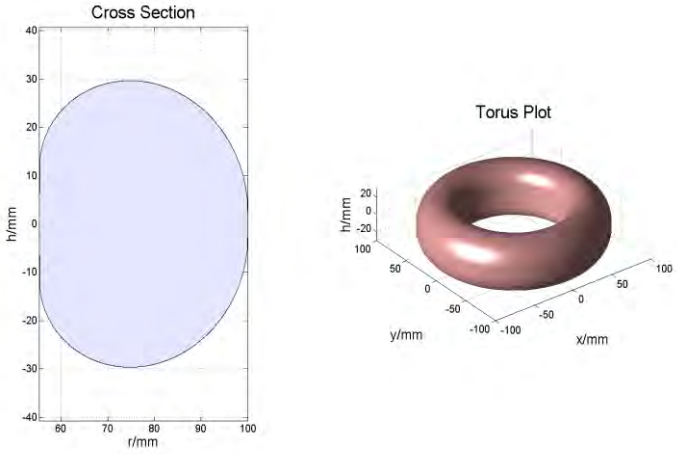

Image 4 A plot of the torus cross section (left) and the 3D shape (right) with MATLAB for the given parameters

As Murgatroyd algorithm assumes that the coil wire is of zero thickness the shape is not optimal for non zero wire thickness. This leads to inaccuracies in the calculation and optimization of the coil and the inductance itself. Furthermore, there are geometrical issues that tend to complicate the winding process. For the coil we choose the parameter $\alpha_i = 4$. Therewith, there are four overlapping layers on the inside when each winding on the torus outside is directly next to each other (see image 5). Taking this into account a decisive geometrical parameter in addition to the in [5] mentioned ratio between inner and outer radius of toroidal shape α the ratio between the innermost that means the radius of every forth winding and the outer radius of the shape. Thus, the MATLAB script has to be modified, else the winding is no more feasible.

Neglecting the effects of eddy-current on the inductance of an air-cored coil it can generally be calculated by

$$L = \frac{\mu_0 N}{\pi} \int_{R_1}^{R_2} \frac{z(r)}{r}\, dr \qquad (1)$$

with N as the number of windings, $z(r)$ as the height (parallel to the rotational axis) and r as the perpendicular distance to the z-axis.

Based on this formula one can estimate the coil inductance to be higher because of single windings including partially larger cross sections than $z(r)$, which merely describes the contours of the shape that is belted by the wire. Additionally, due to the fact that the windings are overlapping R_1 is varying notably. This contributes to a higher inductance.

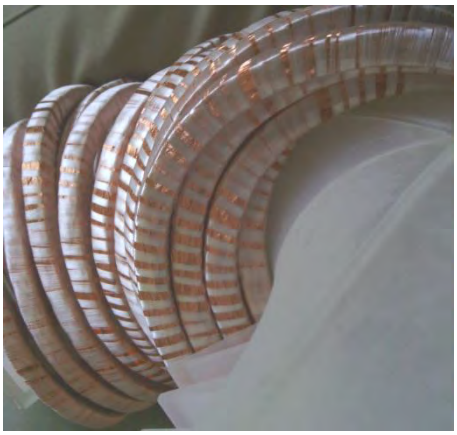

Image 5 Contour of the torus winding with four overlapping litz wires on the inside.

The calculated torus shape has an outer radius R_2 of 14.9 cm and therefore wih $\alpha_i = 4$ an innermost radius (the toroidal radius of every forth winding) of 37.25 mm. The calculations imply an inductance L of at least 108.30 µH and $N = 104$ windings. As the cross section perimeter can be calculated by

$$l_1 = 2\int_{R_1}^{R_2} \sqrt{1+s}\; dr + 2[z(R_1) + z(R_2)] \qquad (2)$$

with $s = dz/dr$ leading to a wire length of at least $l = N \cdot l_1 = 25.984$ m. In fact due to overlapping, the spiral winding geometry and non-zero thickness of the wire the actual length will be larger.

1.3 Litz wire parameters and modeling of the 3D CAD shape

There are two major facts one has to take into account when choosing an adequate litz wire type. The ohmic resistance is in the first place determined by the effective cross section that contributes to the current flow.

That means that the overall cross section has to be chosen sufficiently large as the DC resistance R_{DC} is inversely proportional to the cross section of the conductor. On the other hand, it is necessary to use thin strands inside the wire to stem the skin effect. The effective skin depth δ is following

$$\delta = \frac{1}{\sqrt{\pi f \sigma \mu}} \qquad (3)$$

with $\sigma = 58 \cdot 10^6$ S·m^{-1} as the conductivity of copper and $\mu = \mu_0$ at 25 kHz is 417.6 µm. That means that the radii of a single strand of the litz wire must not exceed that value or get even close to it, else the resistance is expected to be significantly higher than in the DC case.

The litz wire material that is used for this coil has a square cross section with an edge length of 7.5 mm and a strand diameter of 63 µm, which is distinctly below the effective skin depth. It contains 10.000 strands, which results in an effective cross section of 0.31 cm^2.

To facilitate the winding triangular shapes are implemented on the inside of the toroid. Their height corresponds to a stack of four litz wires above each other. Furthermore, there are seperators on the outside to make sure the windings are arranged in a defined way.

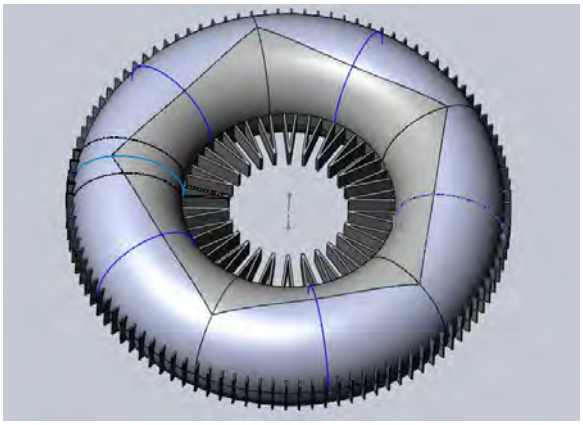

Image 6 3D CAD model of the toroid in SolidWorks with auxiliary triangles on the inside and dividers on the outside

To do a coarse prediction of the DC resistance we need to estimate the length of the wire. As above mensioned the perimeter of the cross section times the number of winding is not sufficient to imply the wire length accurately. Measuring the wire length we obtained approximately 35 m. Following

$$R = R' \cdot l = \frac{l}{\sigma \cdot A} \tag{4}$$

with A as the conducting cross section an ohmic DC resistance of $R = 19.36$ mΩ respectively a resistance per length of $R' = 0.553$ mΩ/m can be predicted. Former measurements with the same litz wire yielded $R' = 0.69$ mΩ/m. Therefore a resistance of $R = 24.15$ mΩ would be implied.
Furthermore at higher frequencies pararisticaly capacitive effects evoke resonance.

3 Results

The toroidal coil is measured with the LCR meter *E4980A* by *Agilent* and validated by the network analyzer *4149A* by HP. The values of interest are the inductance L_S and the ohmic resistance R_S of the coil. Both measuring instruments provide an inductance of 164 µH and a resistance of 23.9 mΩ at low frequencies (< 10 kHz) and 47 mΩ at 25 kHz, which leads to a quality factor of $Q = 550$. The resonant frequency measured by the network analyzer is 2.17 MHz.

4 Discussion

The coil exhibits a high inductance and a sufficiently large quality factor. One things to be optimized is an algorithm that regards the wire thickness.
On the one hand, this would fit the calculated inductance more accurate to the actual one and could also be used to improve the cross section optimization.
The resonant frequency is with more than 2 MHz far beyond the applied frequency in the sending path and therefore sufficiently high. The expected power losses leading to heat emergence are low enough to relinquish active cooling.

Image 7 Toroidal coil with 104 windings of a 7.5 mm thick litz wire resulting in an inductance of 164µH and 43mΩ at 25kHz.

4 Acknowledgement

The authors gratefully acknowledge the financial support of the German Federal Ministry of Education and Research (BMBF) under the grant number 13N11090 as well as the European Union and the State Schleswig-Holstein with the Program for the Future-Economy under grant 122-10-004.

5 References

[1] B. Gleich and J. Weizenecker: Tomographic imaging using the nonlinear response of magnetic particles, Nature, Vol. 435, pp. 1214-1217, 2005

[2] M. Graeser, T. Knopp, M. Gruettner, T.F. Sattel: Analog receive signal processing for magnetic particle imaging, Medical Physics, Vol. 40, No. 4, 2012

[3] T.M. Buzug, S. Biederer, T. Knopp, T.F. Sattel, K. Lüdtke-Buzug: Magnetic Particle Imaging - Challenges and Promises of a New Modality, IFMBE Proceedings, Vol. 25, pp. 1471-1474, 2009

[4] M. Erbe, T.F. Sattel, T. Buzug: Improved field free line magnetic particle imaging using saddle coils, pp 577-582, Biomed Tech 2013

[5] P.N. Murgatroyd: Some optimum shapes for toroidal inductors, IEE PROC., Vol. 129, pp. 168-176, 1982
http://www.mathworks.de/products/matlab/

[6] Filter Free 2011, filter synthesis software, http://www.nuhertz.com/index.php/software

Magnetorelaxation of superparamagnetic nanoparticles studied by atomic magnetometry.

V. Lebedev, V. Dolgovskiy, S. Colombo, B. Michen, A. Fink, A. Weis, University of Fribourg, Fribourg, Switzerland, victor.lebedev@unifr.ch

Introduction

Superparamagnetic nanoparticles (SPIONs) are actively developed and studied as markers and treatment agents in biomedical applications. The specific decay of their magnetization depends on the material properties and the host medium. We report on magnetorelaxation (MRX) investigations of immobilized SPIONs using atomic magnetometers.

Methods

Maghemite SPIONs were produced in-house by thermal decomposition of iron oleate complexes and dried to yield compact samples with various SPION content, and a polydispersity varying over a broad range. In addition we studied Ocean Nanotech SPIONs with narrow size distributions and different mean radii. The relaxation of the magnetized samples was detected by a gradiometer of Cs vapour magnetometers with ms time resolution and sub-nT sensitivity. Data were analysed within the Néel-Brown formalism, accounting for magnetization field strength and duration as well as (TEM-measured) particle size distributions.

Results

For all samples we found that the magnetization decay is very well described by model predictions based on size distributions. The anisotropy constant and saturation magnetization were obtained from model fits to the experimental data, delivering mutually compatible values for all particles within a 10% uncertainty that agree with literature values. For strongly polydisperse samples only a specific narrow-sized subrange effectively contributes to the MRX signals under our experimental conditions. We find a proportionality of the MRX signal amplitude to the mass fraction of the particles within that subrange.

Conclusion

We have shown that different types of SPION samples can be characterized with high accuracy by sensitive atomic magnetometers. The demonstrated combination of measurement and analysis techniques can be used to optimize conditions and materials for MRX experiments.

Data acquisition system with 200 kHz sampling rate for new designs of biomagnetic signal detection

W. Müller[1], P. Grunwald[2], S. Knappe[3], T.H. Sander[1], M. Burghoff[1]

[1] Physikalisch-Technische Bundesanstalt, Berlin, Germany
[2] LAY Audiotechnik, Berlin, Germany
[3] National Institute of Standards and Technology, Boulder, USA
Wolfgang.mueller@ptb.de

Introduction

Non-invasively measured biomagnetic signals of the human body do not exceed frequencies above 1.5 kHz and data acquisition systems with sampling rates of up to 5 kHz are sufficient. Newer designs such as optically pumped magnetometers (OPM) requiring software lock-in amplification need sampling rates in the tenth of kHz. Here a multichannel data acquisition system (DAQ) with high sampling rates is introduced.

Methods

The DAQ uses digital signal processor (DSP) controlled modules and it is scalable up to 512 channels. Each module consists of 16 channels, which are controlled over LAN by the supervisor PC. Additionally, one or several synchronization modules are added to the system. In this way, sampling rates up to 200 kHz can be realized at a sync error < 5 ns (inter-channel delay plus jitter). For low acquisition rates the DSP on each module decimates the primary data after digital lowpass filtering.

Results

Using a prior version of the data acquisition system, signals from OPMs were recorded at a sampling rate of 20 kHz. In parallel hardware lock-in amplifiers were connected and their output recorded together with the raw OPM signals.
Then a suitable lock-in calculation was programmed in Matlab™ and the raw sensor signals were processed and compared with the hardware lock-in output.

Conclusion

We have demonstrated that a data acquisition system with a sufficiently high sampling rate together with an off-line calculation can replace a hardware lock-in amplifier. In future, spatially resolved magnetorelaxometry with fast relaxation curves will be recorded at high sampling rates.

Assessing the applicability of electromagnetic tracking for maxillofacial and orthopaedic surgery

Auer C., Kallus S., Nova I., Eisenmann U., Dickhaus H., University of Heidelberg, Heidelberg, Germany
Christoph.Auer@med.uni-heidelberg.de

Introduction

The susceptibility of electromagnetic tracking (EMT) to distortions induced by metallic objects currently restricts practical capabilities for high-precision surgery. Previous research on measurement error has provided hardly generalizable results. Working towards navigation assistance of orthopaedic and maxillofacial surgery in confined operating areas, we developed an enhanced measurement phantom and protocol adapted from Hummel et. al. and analysed 3D spatial error in real OR setups.

Methods

Our rigid polycarbonate measurement phantom resembles an overturnable three shelf rack of equidistant planes. Each plane holds a grid of 5x5 machine drilled holes, spaced precisely 110mm apart. A pluggable two-pin sensor-mount carrying three orthogonally arranged 6-DOF sensors is used to carry out the position and orientation measurements (40 per plane, repeated three times). For measurement, an NDI Aurora V2 planar field generator was placed in variable positions. By ranking the fiducial registration error (FRE) of local template registrations to matching measurement positions, we obtained static 3D vector fields representing absolute position deviations.

Results

Local registrations with lowest FREs were stable within our measurement series, but often inconsistent across different sensor orientations. In proximity to metal components, the 95% percentile of absolute deviations approached 24.5mm globally and 9.1mm in a suitable subvolume, which are distinct from commonly stated relative errors. Appropriate modifications to generator placement yielded reasonable results of 4.7mm and 2.0mm respectively. Sensors oriented perpendicular to the generator plane performed far worse than those axially parallel. Each measurement cycle involving 6 planes took about 45 minutes to complete.

Conclusion

Our improved phantom design and measurement protocol provides a quick and reliable assessment of 3D measurement deviations by capturing many degrees of freedom at once. Local registration has proven useful to find the best working subvolume and avoids averaging out of substantial deviations. Given the results, we are positive to achieve clinically applicable navigation.

A local TX coil for 3T shoulder imaging

J. Schöpfer[1,2], K. Huber[2], S. Biber[3] and S. Martius[2]
[1] Corporate Technology, Siemens AG, Erlangen, Germany, johanna.schoepfer.ext@siemens.com
[2] LHFT, Friedrich-Alexander-Universität, Erlangen; Germany
[3] Healthcare, Siemens AG, Erlangen, Germany

Abstract

An antenna design of a local TX coil for shoulder imaging is presented, with the promising perspective of significantly reduced RF power requirements compared to standard examinations with the body coil and comparatively low specific absorption rate (SAR). The balance between potential benefits and disadvantages, for instance the inherent B_1^+ field drop of a local surface TX coil, has been examined by simulations with a conducting phantom and a human body model as well as by MRI measurements.

1 Introduction

SAR levels or specified maximum B_1^+ field strengths are common restrictions in 3T MRI imaging leading to either increased scan times or suboptimal image quality. This is of particular interest when imaging patients with metal implants. Improvements can be achieved by local transmit coils that are adapted to the specific body area (e.g. shoulder)

Whereas in ultra-high-field systems (≥7T) local transmit coils are well established to produce the required RF field, in commercially available 3T systems they are not that widely spread except for head and knee coils and few approaches in research. [1] [2]

2 Methods

The transmit coil was designed to be inserted in a commercially available RX shoulder case providing a convenient fit on the shoulder and thereby maintaining the patient comfort.

By various simulation runs a specific number of antenna elements and decoupling methods were evaluated with particular attention to maximum available B_1^+ field strength, B_1^+ homogeneity and SAR values in a predefined area around the shoulder joint. All simulations were done with Microwave Studio (CST, Darmstadt, Germany).

For high B_1^+ efficiency and homogeneity, the TX shoulder coil was designed as a three-element structure with quadrature excitation. Two simultaneously fed elements enclose the shoulder joint from the back and front of the human torso. The third element is arranged orthogonally to the two feeding elements on the side of the shoulder.

The antenna elements were matched to 50Ω at 123.2MHz and decoupled by shared conductors which turned out to be advantageous compared to e.g. decoupling capacitors for different load distances. The simulation model of the shoulder coil and a conducting phantom can be seen in Figure 1, including the FR4 substrate, copper strips with a width of 1cm and 15 lumped port elements in total.

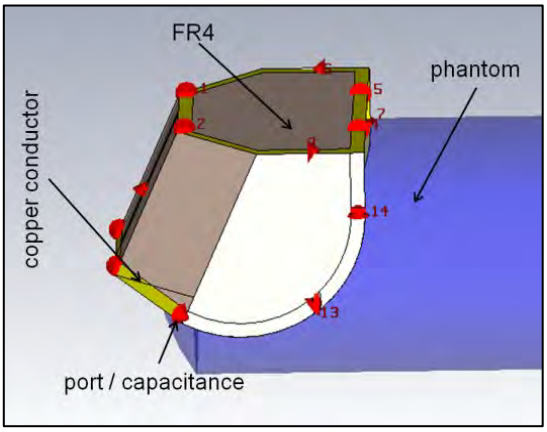

Figure 1: Simulation setup of the shoulder coil on an FR4 substrate and a conducting phantom, simulated with Microwave Studio (CST)

The dimensions of the complete coil structure at its largest were 13cm x 18cm x 21cm, enabling a complete coverage of the shoulder joint.

A co-simulation procedure, similar to [3], was chosen. The ports in the 3D-design of the coil (cf. Figure 1) were replaced by capacitor elements in a circuit simulator (Design Studio, CST) and a matching and feeding network was added. As a result, simulation and matching time of the whole structure could be reduced significantly.

In a second step, a human body model ("Duke" [4]) was included (cf. Figure 2). Accordingly, a more realistic evaluation of the SAR behavior, averaged over 10g human tissue, and the B_1^+ field strength, respectively field distribution of the transmit antenna, could be performed.

An adequate distance between the antenna structure and the shoulder of the human body model was evaluated in various simulation runs by supervising and comparing the SAR behavior and was finally set to 2cm on average.

The simulated antenna array was built up with identical dimensions using copper strips on FR4 substrates and placed on the inner shell of the shoulder coil case (cf. Figure 3).

The two elements arranged parallel on the side of the coil structure were connected via λ/4 coaxial lines arranged as cable traps. Thereby an impedance transformation and combination to a single transmit channel as well as potential mode suppression could be realized.

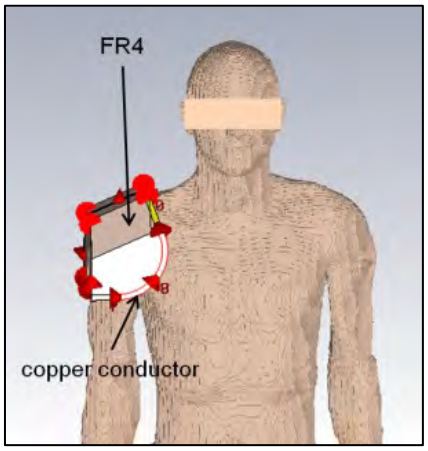

Figure 2: Simulation setup of the shoulder coil on an FR4 substrate and a human body model

Since the transmission behavior and SAR figures of the coil were the main focus of this work, the same coil was also used for receiving and no optimized RX coil, e.g. with higher channel count, was included additionally. In this context, the TX coil hardware was extended by a transmit/receive switch including a preamplifier. A feeding network was added in order to connect the shoulder coil to the local transmit channel of the Siemens MAGNETOM Skyra 3T MRI system.

Figure 3: Hardware setup of the simulated TX shoulder coil including feeding network and RX/TX switch. For simplicity reasons and improved handling during measurements, the housing cover was omitted.

Measurements of the H field components with a pick up loop and a vector network analyzer showed a balanced amplitude of both field components (H_x & H_y) in the center of the shoulder coil and thus no further compensation measures like a weighting of the transmit channels were required. To generate the phase difference of the feeding channels, a quadrature hybrid coupler for high power requirements was designed. Due to the comparatively long wavelength (λ_0=2.4m), it was realized with discrete elements for reduced space requirements in comparison to an implementation with transmission lines [5].

3 Results

Simulations with a conducting phantom and a human body model resulted in an average B_1^+ field of 0.7µT in a predefined area around the joint and local SAR values, per 10g tissue, of 0.8W/kg for 1W input power (cf. Figure 4).

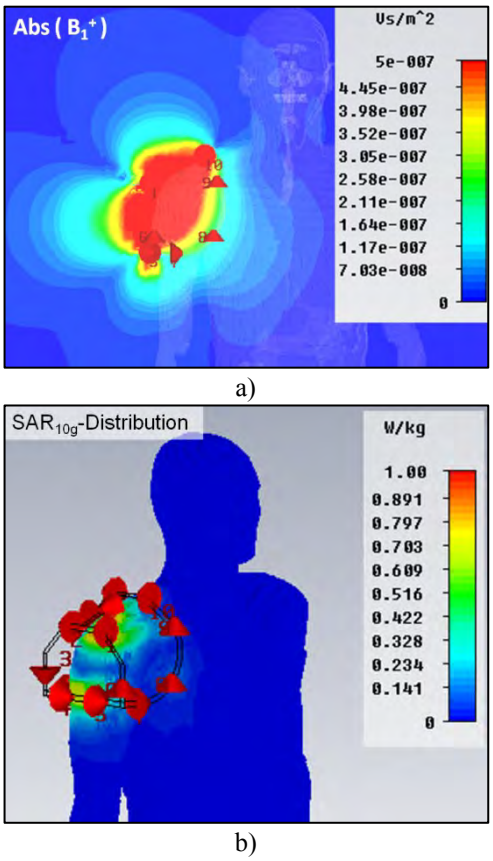

Figure 4: Simulation results with a human body model.
a) B_1^+ field distribution for an input power of 1W
b) SAR distribution averaged over 10g human tissue

In comparison, simulation with the traditional body coil showed enhanced power demands by a factor of 8-15 and increased SAR values depending on the placement of the patient.
Figure 5 shows the measured scattering parameters of the antenna array placed on a phantom with similar conductivity to the simulation setup. s_{11} and s_{22} were below -20dB for different load distances, a corresponding behavior that could also be seen in the simulations. The decoupling of both channels resulted in -13dB and hence was

increased compared to the simulation (s_{21}< -20dB). This could be the effect of slight differences in the phantom placement inside the shoulder coil.

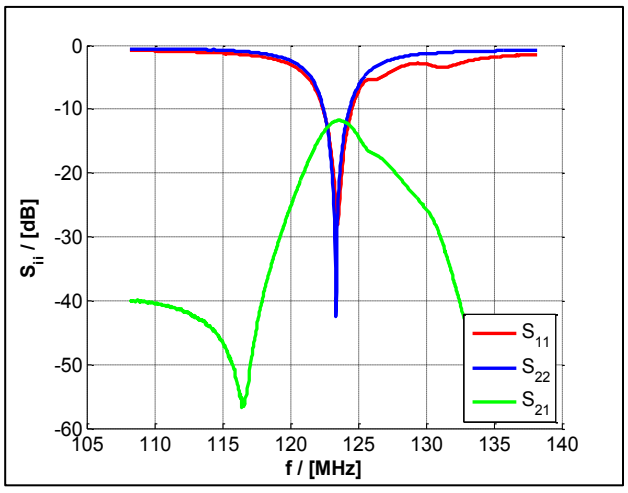

Figure 5: Scattering parameter of the antenna elements, measured with a vector network analyzer

For preliminary measurements, the shoulder coil hardware was tested to be power proof up to 5kW and was integrated in a Siemens MAGNETOM Skyra MRI. The imaging object was chosen to be a pork shoulder (2.5kg) including fat and muscle tissue. The first measurement of a spin-echo sequence can be seen in Figure 6.

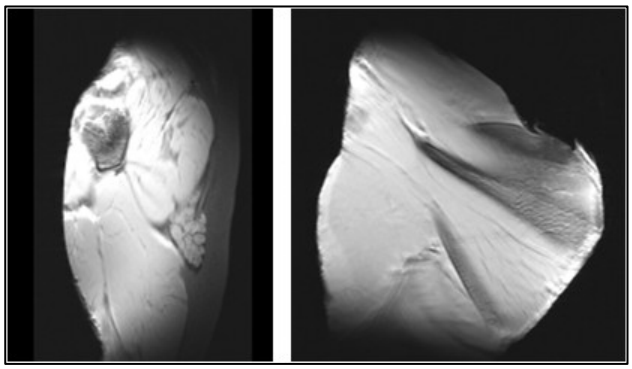

Figure 6: Spin-Echo of a pork shoulder, measured with the local transmit coil (sagital and coronal slice)

The corresponding reference amplitude for an average B_1^+-Field of 11.75µT in the examined object was 82V (eq. 134.5W).
Furthermore, discrete fiber-optic thermo sensors were placed inside the pork shoulder showing no considerable increase in temperature after 30min of heating.

4 Conclusion

The preliminary results show great potential for shoulder imaging with local TX coils. The shoulder coil could be used as an addition to standard examinations with the body coil where high B_1^+ fields occur to be the limiting part of the imaging process. Further improvement could be achieved with the use of extended pulse design methods and will be evaluated in further research steps.

5 References

[1] Wu B., et al: Human Spine Imaging Arrays with Adjustable Inductive Decoupling, IEEE transactions on Biomedical engineering, 2010

[2] Srinivasan R., Lin C., Bernstein M. A.: Transmit/Receive Neck Coil for 3T. Proc. Intl. Soc. Magn. Reson. Med. 10, 2002

[3]Kozlov M., Turner, R.: Fast MRI coil analysis based on 3-D electromagnetic and RF circuit co-simulation: Journal of Magnetic Resonance 200, 2009

[4] Christ A, Kainz W., Hahn W. K., et.al.: The Virtual Family – Development of surface based anatomical Models of Two Adults and Two Children for Dosimetric Simulations: Physics in Medicine and Biology Volume 55 Issue 2; 2010

[5] Bahl I., Bhartia P.: Microwave Solid State Circuit Design, Second Edition: John Wiley & Sons, 2003

T vector cardiography for detection of patients after myocardial infarction

M. Goernig[1], B. Hoeffling[2], S. Lau[3], H.R. Figulla[2], J. Haueisen[3]
[1]Clinic of Geriatrics, HELIOS Klinikum Aue, Germany, Matthias.Goernig@uni-jena.de
[2]Clinic of Internal Medicine I, University Hospital Jena, Germany
[3] Technical University Ilmenau, Germany

Abstract

Electrocardiography (ECG) is widely used to detect myocardial injury. ECGs after subendocardial, non ST-elevation myocardial infarction may lack from striking infarct pattern. T vector cardiography (VCG) involves three-dimensional characterization of the ventricular repolarization and identifies abnormalities as empirically done by eye in conventional ECG - but on an advanced level of analysis. We compared discriminatory performance of VCG to conventional ECG analysis in identifying post myocardial infarction patients. T vector and T loop parameters were compared to infarct indicators of the ECG in 114 subjects: 59 patients (42 males, mean age 54 years) 15 days after myocardial infarction (11.9 ± 6.9d) and 55 healthy controls (27 males, mean age 49 years). ECG infarct indicators in 75.2 % correctly separated patients from controls. T vector and loop parameters were superior to conventional ECG: patients from controls were correctly separated in 83.2 %. Discrimination analyses revealed a sensitivity of 71.7% and a specificity of 88.7% for vector ECG, the conventional analysis had a sensitivity of 66.7% and specificity of 77.4%, respectively. T Vector ECG improves detection of myocardial injury and is applicable for analysis of cardiac repolarization.

1 Introduction

The 12-lead electrocardiogram (ECG) is a standard procedure for the assessment of the status after myocardial infarction (MI). There are typical ECG indicators, which are presented up to live long after MI such as Q-wave, T-wave polarity, R-reduction and ST-segment deviation – as a sign of chronic myocardial injury. These indicators can be missed especially in tiny non ST-elevation MI [1]. T vector cardiography (VCG) involves three-dimensional characterization of the ventricular repolarization and identifies abnormalities as empirically done by eye in conventional ECG - but on an advanced level of analysis.

According to the literature 15 to 20% of patient had silent myocardial infarction especially in diabetes mellitus. These patients are still at risk for reinfarction and sudden cardiac death and should be identified, monitored and treated with secondary prevention medication [2]. Therefore it is necessary to evaluate if VCG- which is as easy as standard ECG done – is a more sensitive non-invasive tool for the diagnostic of tiny myocardial injury.

A correlation between QT-duration in the ECG and the 3-dimensional T vector loop morphology among post MI patients and healthy control subjects was described before. Abnormalities in T vector magnitude and orientation were found to be markers of altered ventricular repolarization in post MI patients [3,4].

In our study we want to prove identification of patients after MI by T vector and loop characteristics compared to ECG, especially those without diagnostic conventional ECG.

2 Methods

2.1. Patients

114 subjects, 59 patients (42 males, mean age 54 years) mean 12 days (11.9 ± 6.9d) after myocardial infarction (MI, angiographic proven and with positive infarct serology) and 55 healthy controls (27 males, mean age 49years) without history of CAD and echocardiographic proven normal left ventricular function were investigated. Patients with atrial fibrillation or pacemakers were excluded.

2.2. ECG

Standard 12 lead ECG was performed in all subjects and the following nine infarct indicators were selected by eye: Q wave > ¼ R-wave in Einthovens- or Wilsons leads, ST deviation in Einhovens- or Wilsons leads (in mV), T wave polarity change in Einhovens- or Wilsons leads (0=normal, 1=preterminal negative, 2=terminal negative 3=terminal negative negative in all leads), R reduction in Wilsons leads (0=normal, 1=R-reduction, 2=R-lost, 3=R-lost in all leads), QRS duration (ms), left bundle branch block (0=normal, 1=left bundle branch block)

2.3. VCG

Continuous VCG recording was performed over 10 min at rest in the supine position. VCG signals were continuously collected from 8 electrodes [5] positioned according to the Frank orthogonal lead system (*X*, *Y*, and *Z*). Signals were recorded at 500 Hz on a standard cardiograph and stored as a digital file. The method has been described in detail elsewhere [5]. At the start of the recording the dominant QRS pattern is automatically determined from the first 10 complexes, which then is used as the template to exclude subsequent artifacts or ectopic ventricular com-

plexes. Signals are averaged every 10 seconds, every averaged complex is compared with the template, and the changes are presented as trend curves over time. Heart rate, QRS, and QT intervals were measured automatically in each averaged complex. For each 10-second period an averaged 3-D T vector loop and the direction of the maximum QRS and T vectors were determined. The T vector and loop morphology was analyzed off-line using a MATLAB routine. The following six T vector parameters and T loop parameters were measured by vectorcardiography as defined elsewere in detail [6]: T vector elevation, T vector azimuth, QRS-T angle, Tarea, Teigenv, Tavplan.

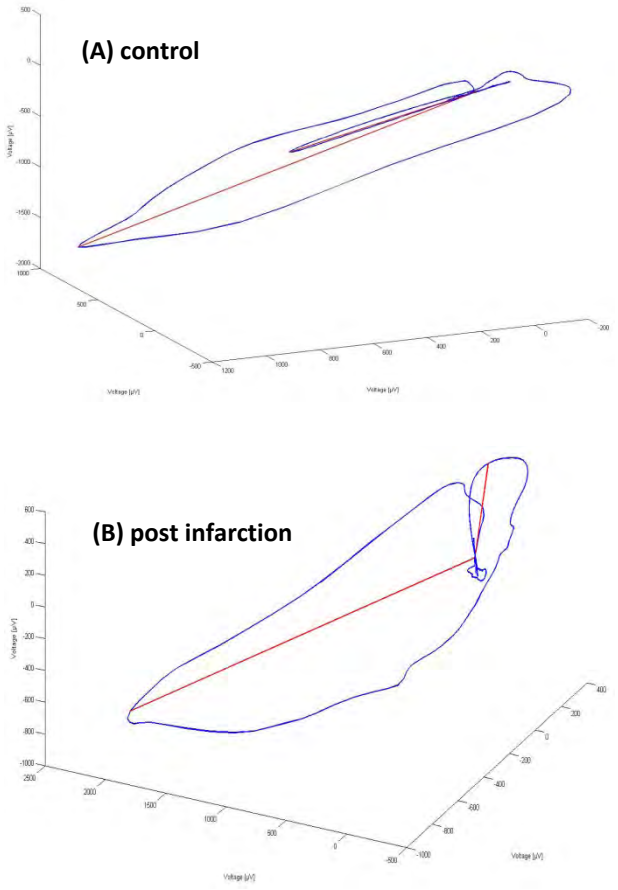

Figure 1 An example for QRS-T angle of a control (A) and a post infarction patient (B) according to [6].

2.4. Statistics

Descriptive statistics, Mann-Whitney U-test for univariate analyses and for evaluation of the discriminatory power of the ECG and MCG parameters to separate the patients with MI and controls stepwise binary logistic regression analyses and discrimination analyses (SPSS 18.0) was used.

3 Results

Five of the nine ECG infarct parameters (table 1) and five of the six T vector and loop parameters were significantly different in MI patients and controls (table 2). Using stepwise binary logistic regression ECG analysis 75.2% of the patients could be classified correctly - combining the best two ECG classifiers (T polarity in Einthovens- and ST deviation in Wilsons leads) and was not improving by further combination.

Stepwise binary logistic regression analyses of the VCA parameters could separate the groups in 83.2% combining the best two classifiers (Tarea, T vector azimuth).

VCA parameters could separate the two groups with a sensitivity of 71.7% and a specificity of 88.7%, whereas the infarct signs of the ECG had a sensitivity of 66.7% and a specificity of 77.4%..

Table 1 Descriptive statistics and univariate significances (Mann-Whitney U test, significance p<0.05, high significance p<0.01) of ECG infarct parameters and patients with myocardial infarction and controls (MI and CON); mv – mean value; sd – standard deviation.

	MI; N=59	CON; N=55		
ECG parameter	mv±sd	mv±sd		p value
R-reduktion Wilsons	0.92±0.91	0.58±0.77	*	0.046
T-polarity Einthovens	1.25±0.88	0.49±0.68	**	0.001
Q-wave Einthovens	0.74±0.68	0.49±0.56	*	0.042
ST-deviation Einthoven (mV)	0. 04±0.10	<0.01±0.05	*	0.045
ST-deviation Wilsons (mV)	0. 14±0.23	0.04±0.06	**	<0.001

Table 2 Descriptive statistics and univariate significances (Mann-Whitney U test, significance p<0.05, high significance p<0.01) of T vector and loop characteristics in patients with myocardial infarction ad controls (MI and CON); mv – mean value; sd – standard deviation.

T vector and loop	MI; N=59	CON; N=55		
characteristics	mv±sd	mv±sd		p value
T vector azimuth	114.16±27.94	129.60±19.89	**	0,001
QRS-T angle	30.04±28.75	80.46±48.89	**	<0.001
Tarea	4.39±5.45	5.32±2,22	**	0,001
Tavplan	6.22±4.98	4.18±2.47	*	0,054
Teigenv	0.86±0.11	0.95±0,07	**	<0,001

4 Conclusion

T vector and loop characteristics improves the discriminatory power of conventional ECG infarct parameters to separate patients after MI and controls. Vectorcardiography is able to analyse homogeneity of cardiac de- and repolarisation. VCA involves full 3D spatiotemporal information to identify de- and repolarization abnormalities as empirically done by eye in conventional ECG analysis - but on an advanced level of analysis.

5 References

[1] Gomez JF, Zareba W, Moss AJ, McNitt S, Hall WJ. Prognostic value of location and type of myocardial infarction in the setting of advanced left ventricular dysfunction. Am J Cardiol. 2007 Mar 1;99:642-6. 2007

[2] Valensi P, Lorgis L, Cottin Y. Prevalence, incidence, predictive factors and prognosis of silent myocardial infarction: a review of the literature. Arch Cardiovasc Dis 2011;104 (3): 178–88
[3] Vahedi F, Haney MF, Jensen SM, Näslund U, Bergfeldt L. Effect of heart rate on ventricular repolarization in healthy individuals applying vectorcardiographic T vector and T vector loop analysis. Ann Noninvasive Electrocardiol. 2011;16(3):287-94
[4] Rubulis A, Bergfeldt L, Rydén L, Jensen J. Prediction of cardiovascular death and myocardial infarction by the QRS-T angle and T vector loop morphology after angioplasty in stable angina pectoris: an 8-year follow-up. J Electrocardiol. 2010;43(4):310-7
[5] Sederholm M, Erhardt L, Sjogren A. Continuous vectorcardiography in acute myocardial infarction. Natural course of ST and QRS vectors. Int J Cardiol 1983;4:53–63
[6] Rubulis A, Jensen J, Lundahl G, Tapanainen J, Wecke L, Bergfeldt L.T vector and loop characteristics in coronary artery disease and during acute ischemia. Heart Rhythm. 2004;1(3):317-25

Superparamagnetic Coatings for Magnetic Particle Imaging

K. Lüdtke-Buzug, C. Debbeler
Institute of Medical Engineering, Universität zu Lübeck, Lübeck, Germany,
E-Mail: luedtke-buzug@imt.uni-luebeck.de

Abstract

Magnetic Particle Imaging (MPI) is a novel imaging method with high potential in a variety of interesting medical applications. However, a bottleneck in MPI is the availability of optimal tracer material, the so-called SPIONs (superparamagnetic iron oxide nanoparticles). In this contribution, we focus on techniques to prepare surgical instruments for visualization in MPI. In a first study, commercially available metallic anti-rust paints are used to coat PE films. In a second study, self-synthesized SPIONs have been suspended into acrylic paints and dried onto PE films. The films of both studies were analyzed with MPS (magnetic particle spectroscopy), where materials are subjected to a dynamic magnetic field. In conclusion, the coatings based on self-synthesized SPIONs show a superior magnetic behavior compared to commercial anti-rust coatings.

1 Introduction

Magnetic Particle Imaging (MPI) is a new imaging modality invented in 2001 [1] and first published in 2005 [2]. MPI fulfils the most important criteria of a successful imaging technique, i. e. a high spatial resolution, a high sensitivity, and a real-time capability. Additionally, it comes without a radiological dose and promises quantitative measurements. In combination, MPI is setting the benchmark for the future.

MPI images the spatial distribution of particles with a magnetic core, or, more precise, superparamagnetic iron oxide nanoparticles (SPIONs). The technical concept of MPI is based on physical characteristics of the SPIONs, i. e. a non-linear magnetization behavior and a pronounced saturation regime. The non-linearity is the signal generating feature. If the SPIONs are subjected to a sinusoidal magnetic field, they will react with a non-linear distortion of the sinusoidal excitation [2-4]. This will be explained in detail in Section 2.

As indicated above, the tracer material, i. e. the SPIONs, plays a key role in MPI. Recently, the effectiveness of SPION-enhanced MRI has been shown in several clinical trials for human lymphography and the characterization of hepatosplenic tumors [5,6]. Additionally, studies have been carried out with SPIONs for the detection of macrophages. This has been done in animal models in the context of different diseases of the central nervous system including inflammation, tumors, or ischemia, in bone marrow alterations and arteriosclerotic plaques [7-9]. For MPI, clinical application scenarios have been suggested as well. For instance, in sentinel lymph node biopsy (SLNB), the SPIONs could be a surrogate for the radioactive tracer used today [10,11]. However, it has also been shown, that the commercially available tracer material is not optimal for the requirements of MPI [12,13].

In this paper, the development of superparamagnetic iron oxide nanoparticles (SPIONs) dispersed in polymers is described. This opens a wide field of potential applications. For instance, it is common practice to use coatings for material protection against corrosion or against aging.

However, with our approach of superparamagnetic coatings we pursue a different aim. Our coatings are used for varnishing medical instruments to be used in MPI. In particular, the coating of catheters is an application of interest. Usually catheters are inserted into vessels, for instance, into the saphenous vein of the patient.

Today, this procedure is carried out in the catheter lab under radiological control, i.e. X-ray guidance. To avoid X-ray dose, superparamagnetic coatings of endoscopes or catheters are an appropriate alternative and would allow for MPI-guided minimally invasive surgical interventions.

2 Methods and Materials

2.1 Methods

2.1.1 Spectrometer Measurements

In this contribution, experiments with metallic anti-rust protection coatings and new developed coatings with self-synthesized SPIONs will be presented. The analysis of the novel coatings has been carried out with a proprietary magnetic particle spectrometer (MPS, Image 1).

The MPS used here, consists of a coil set-up that produces a static and sinusoidally varying magnetic field (Image 2).

Table 1 Parameter settings for MPS measurements

Spectroscopic measurement conditions	
Field strength	20 mT
Periods	10
Repetitions	12500
Frequency	25 kHz

The nanoparticles under investigation are subjected to these fields and their re-magnetization dynamics charac-

terizes the particle quality with respect to magnetic particle imaging (MPI). The parameters of the MPS are given in Table 1.

Image 1 Magnetic particle spectrometer MPS (Fork Labs project @ University of Lübeck).

As shown in Image 2, MPS is based on the non-linear magnetization characteristic of the SPIONs. When the magnetic nanoparticles are subjected to a time varying magnetic field $H_D(t)=H_0 \sin(2\pi f_0 t)$, a re-magnetization dynamic $M(H(t))$ is observed. Due to the non-linearity of the magnetization characteristic, i. e. the curve $M(H)$, the frequency spectrum of the magnetization response does not only consists of the base frequency f_0 of the excitation, but also of the odd integer multiples of f_0, called higher harmonics.

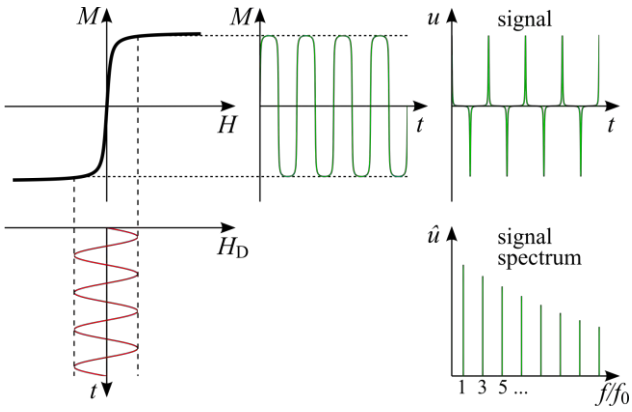

Image 2 Re-magnetization dynamics of superparamagnetic nanoparticles subjected to a sinusoidally varying magnetic field (adapted from [5]).

The behavior shown in Image 2 can be modelled by the Langevin theory of paramagnetism. Here, the magnetization curve $M(H)$ of the particles is described by $M(t) = m_s c\,(\coth(\xi)-\xi^{-1})$ with $\xi = m_s \mu_o H(t)/(k_B T)$, where μ_o denotes the permeability of vacuum, k_B the Boltzmann constant, T the temperature in Kelvin, c the particle concentration, and $m_s=1/6\pi D_c^3 M_s$ the magnetic moment of the particles at saturation.

It is important to note, that the particles can be characterized by their magnetic core diameter D_c and the saturation magnetization M_s (e. g. 0.6 T/μ_0 for magnetite). For the spectrometer design it is assumed that the concentration c of the nanoparticles is homogeneous within the sample.

Furthermore, the magnetic field $H(t)$ is also homogeneous in the sample chamber and has only one spatial component. This can be achieved by using a solenoid coil to generate the magnetic field, where the sample chamber lays inside the coil. The sample chamber of the spectrometer is chosen as a cylinder with a diameter of 5 mm and a length of 5 mm to fit a cylindrical tube with samples of a volume up to 100 µl.

The variance of the magnetic field $H(t)$ within the sample chamber is set to be smaller than 0.2 %. This can be achieved by a solenoid transmit coil with a diameter of 40 mm, a length of 60 mm, and 40 windings. The receive coil is placed close to the sample chamber. It has a diameter of 20 mm, a length of 10 mm, and 20 windings. Both coils are mounted concentrically to the sample chamber [14].

2.2 Materials

2.2.1 Commercial coatings

The three following commercially available anti-rust coatings have been used: (a) *Metall-Schutzlack matt Schwarz* (*Hammerite*) as coating varnish, (b) *Auto Color Acryl Spray* (*Dupli-Color*), and (c) *Rust protection 2000 Plus* (*Weicon*); (b,c) as sprays.

In a first experiment, the metallic anti-rust coatings were transferred onto PET layers and dried.

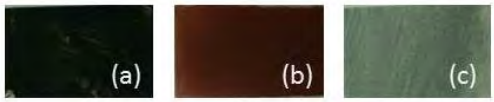

Image 3 Three different commercial anti-rust coatings dried on PE films. (a) *Metall-Schutzlack matt Schwarz (Hammerite),* (b) *Auto Color Acryl Spray (Dupli-Color), and* (c) *Rust protection 2000 Plus (Weicon)*

These coated layers are cut in appropriate pieces to fit the measurement chamber of the MPS (see Section 2.1.1).

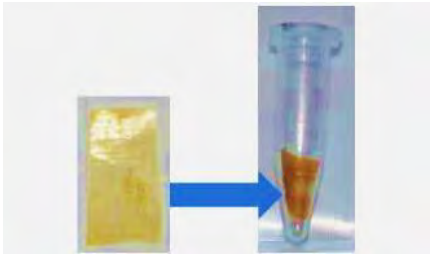

Image 4 Coating, dried on PE films and placed in an Eppendorf cup in preparation for MPS measurements.

2.2.2 Self-synthesized coatings

In a second series of experiments, self-synthesized water-solved superparamagnetic iron oxide nanoparticles combined with different synthetic acrylic paint (*PROFIDUR Klarlack* and *Duracryl Klarlack*, both *SCHÖNER WOHNEN*) have been used.

Image 5 Self-synthesized coating dried on PE layer

PROFIDUR is a water-dilutable acrylic resin, which also contains silicates, isoparaffin and additives (Ch 235939X). *Duracryl* is a acrylate dispersion free of aromatic compounds. Solvents are water and glycols. Furthermore, *Duracryl* contains, as *Profidur*, additives and, supplementary, preserving agents such as methyl- and benzisothiazolion (Ch 231755).

The great advantage of the self-synthesized particles are their good suitability for MPI in comparison to tracers available on the market [12].

To obtain a homogenous particle dispersion, the nanoparticles have to be transferred to the polymer in a fast process and the dispersion has to be homogenized by vigorous stirring. Consecutively, the homogenized mixture of nanoparticle-enriched varnish must be dried instantaneously while applied to the surface materials.

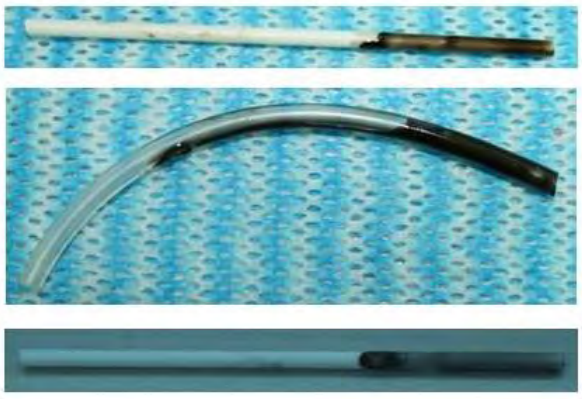

Image 6 Self-synthesized coating dried on PE tubes

In this work, PE layers (Image 5) and other tubing materials (Image 6) have been used. Again, MPS measurements have been carried out to analyze the coatings. Finally, the results of the measurements of the commercial coatings were compared with the novel coating approaches.

3 Results

To make sure that the pure synthetic acrylic paint (i. e. the particle-free matrix) gave no spurious MPI signals, it was measured with the MPS under the same conditions as all other samples. Image 7 shows the comparison of the pure acrylic paint and the acrylic paint mixed with particles.

The commercial metallic anti-rust protection coatings show a weak magnetic response in the MPS measurements. In contrast, the response of the novel acrylic-based nanoparticle coatings showed an appropriate MPS signal (Image 8a) that promises applicability for MPI.

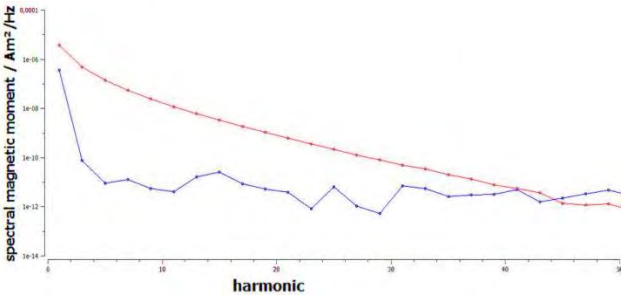

Image 7 Spectrum of the magnetic response of self-synthesized coatings and acrylic paint without particles (● self-synthesized coating, ● *ProfiDur* without particles)

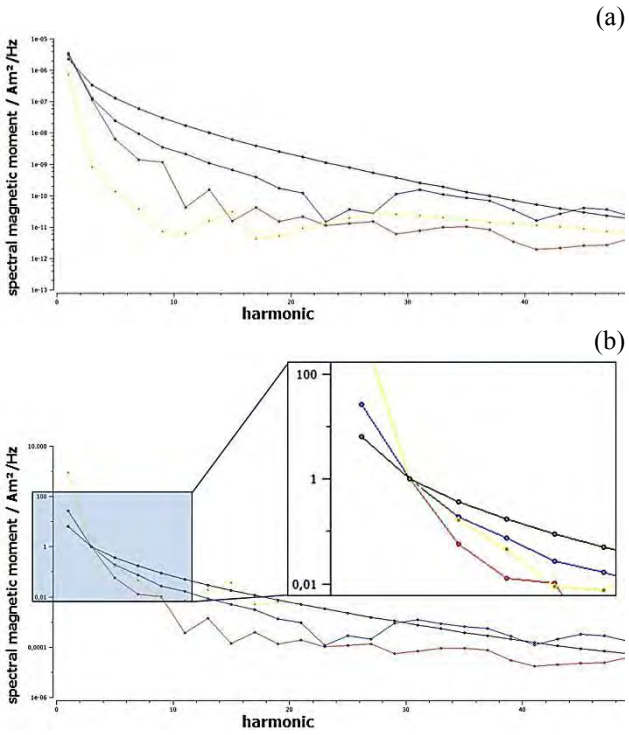

Image 8 Spectrum of the magnetic response of anti-rust and self-synthesized coatings. (a) Not normalized and (b) normalized to the third harmonic. (● *Metall-Schutzlack matt Schwarz (Hammerite),* ● *Auto Color Acryl Spray (Dupli-Color), and* ● *Rust protection 2000 Plus (Weicon),* ● *self-synthesized coating)*

Additionally, the MPS results of different materials (Image 8b) have been normalized to the third harmonic. In comparison, the signal of the acryl-based coating (black curve) is superior to the commercial material by on order in magnitude for at least an interval of 30 hamonics.

4 Conclusion

It can be demonstrated that commercial metallic anti-rust protection coatings (*Metall-Schutzlack*, *Hammerite*; *Auto Color Acryl Spray*, *Dupli-Color*; *Rust protection 2000 Plus*, *Weicon*) show a poor magnetic response in MPS measurements. From a technical point of view, these materials seem to be inappropriate for coating of surgical instruments in MPI-guided interventions.

On the other hand, novel acrylic-based nanoparticle coatings result in an acceptable magnetization signal in MPS measurements. From a medical point of view, however, special attention has to be paid to biocompatibility when selecting a nanoparticle matrix for magnetic coatings to be transferred onto surfaces of surgical instruments. In particular, the commercial anti-rust protection coatings cannot be used as coating in medical applications due to their bioincompatibility.

Nevertheless, these materials, applied as structured SPION coatings, may find applications as security labels or fraud-resistant badges in security-sensitive areas. To improve biocompatibility, superparamagnetic nanoparticles may be combined with synthetic polymers, such as poly(tetrafluoroethylene) or polyethylene, for instrument coatings.

References

[1] Gleich, B.: Method of determining the spatial distribution of magnetic particles, Publication Number: US20030085703 A1, Application Number: US 10/270,991, Filed: 15. Okt. 2002, Priority Date: 19. Okt. 2001

[2] Gleich, B., Weizenecker, J.: Tomographic imaging using the nonlinear response of magnetic particles, Nature, 435, pp. 1214-1217, 2005

[3] Buzug, T. M., Bringout, G., Erbe, M., Gräfe, K., Graeser, M., Grüttner, M., Halkola, A., Sattel, T. F., Tenner, W., Wojtczyk, H., Hägele, J., Vogt, F. M., Barkhausen, J., and Lüdtke-Buzug, K.: Magnetic Particle Imaging: Introduction to Imaging and Hardware Realization. Z Med Phys, vol. 22, no. 4, pp. 323-334, 2012

[4] Duschka, R. L., Haegele, J., Panagiotopoulos, N., Wojtczyk, H., Barkhausen, J., Vogt, F. M., Buzug, T. M., and Lüdtke-Buzug, K.: Fundamentals and Potential of Magnetic Particle Imaging. Current Cardiovascular Imaging Reports, vol. 6, no. 5, pp. 390-398, 2013, doi: 10.1007/s12410-013-9217-1

[5] Weissleder R, Hahn P F, Stark D D et al.: Superparamagnetic iron oxide: enhanced detection of focal splenic tumors with MR imaging. Radiology 1988; 169: 399-403

[6] Bellin M F, Roy C, Kinkel K et al.: Lymph node metastases: safety and effectiveness of MR imaging with ultrasmall superparamagnetic iron oxide particles--initial clinical experience. Radiology 1998; 207: 799-808

[7] Seneterre E, Weissleder R, Jaramillo D et al.: Bone marrow: ultrasmall superparamagnetic iron oxide for MR imaging. Radiology 1991; 179: 529-533

[8] Fleige G, Nolte C, Synowitz M et al.: Magnetic labeling of activated microglia in experimental gliomas. Neoplasia 2001; 3: 489-499

[9] Ruehm S G, Corot C, Vogt P et al.: Magnetic resonance imaging of atherosclerotic plaque with ultrasmall superparamagnetic particles of iron oxide in hyperlipidemic rabbits. Circulation 2001; 103: 415-422

[10] Finas, D., Baumann, K., Sydow, L., Heinrich, K., Gräfe, K., Lüdtke-Buzug, K., and Buzug, T. M.: Lymphatic Tissue and Superparamagnetic Nanoparticles - Magnetic Particle Imaging for Detection and Distribution in a Breast Cancer Model. Biomedical Engineering, vol. 58, Suppl. 1, 2013, doi: 10.1515/bmt-2013-4262

[11] Ruhland, B.; Baumann, K.; Knopp, T.; Sattel, T., Biederer, S.; Lüdtke-Buzug, K.; Buzug, T.; Diedrich, K.; Finas, D.: Magnetic Particle Imaging with Superparamagnetic Nanoparticles for sentinel lymph node detection in breast cancer. Geburtshilfe und Frauenheilkunde, 69(8), p. 758, 2009

[12] Lüdtke-Buzug, K., Haegele, J., Biederer, S., Sattel, T. F., Erbe, M., Duschka, R. L., Barkhausen, J., and Vogt, F. M.: Comparison of commercial iron oxide-based MRI contrast agents with synthesized high-performance MPI tracers. Biomedical Engineering, vol. 58, no. 6, pp. 527-533, 2013, doi: 10.1515/bmt-2012-0059

[13] Lüdtke-Buzug, K.: From Synthesis to clinical Application. Magnetic Nanoparticles. Chemie in unserer Zeit, 46(1), pp. 32-39, 2012

[14] Biederer, S., Knopp, T., Sattel, T. F., Lüdtke-Buzug, K., Gleich, B., Weizenecker, J., Borgert, J., and Buzug, T. M.: Magnetization Response Spectroscopy of Superparamagnetic Nanoparticles for Magnetic Particle Imaging. Journal of Physics D: Applied Physics, vol. 42, no. 20, 2009

A Cotton-Mouton Spectrometer with Optimized Field Cancellation Using n-MOSFET-Based Current Switching

R. F. Knobloch, C. Debbeler, and K. Lüdtke-Buzug
Institute of Medical Engineering, Universität zu Lübeck, Lübeck, Germany, luedtke-buzug@imt.uni-luebeck.de

Abstract

Superparamagnetic iron oxide nanoparticles (SPIONs) are used in a variety of medical applications, for example as contrast agents in hyperthermia and magnetic resonance imaging (MRI). Another novel application is the use of SPIONs as tracer in magnetic particle imaging (MPI). Especially for medical applications, the hydrodynamic diameter of the tracers is a crucial factor. The Cotton-Mouton spectrometer (CMS) is a method of measuring the hydrodynamic particle diameter d_h using the Cotton-Mouton effect (CME). The CME induces a birefringence in ferrofluids by a magnetic field. The particle diameter is estimated by measuring the time constant of the Brownian relaxation. In this paper, the influence of generation and cancellation of the magnetic nanoparticle saturation using current switching by a metal-oxide-semiconductor field-effect transistor (MOSFET) is studied.

1 Introduction

Medical imaging techniques have been revolutionized in the last decades. In combination with contrast agents, which enhance image contrast significantly, new diagnostic insights have been gained. This includes state of the art techniques as ultrasound [1], computed tomography [2], and magnetic resonance imaging (MRI) [3].

In 2005, Gleich and Weizenecker introduced magnetic particle imaging (MPI), which promises a higher sensitivity than MRI [4]. With MPI the spatial distribution of superparamagnetic iron oxide nanoparticles (SPIONs) in a volume is determined. Another important medical application of SPIONs is, for instance, magnetic hyperthermia treatment for cancer.

For both applications the knowledge of the exact particle parameters is a crucial point, since the size of particles influences the energy absorption in hyperthermia [5] and the image quality in MPI [6,7].

Another crucial parameter in medical applications is the hydrodynamic diameter d_h of the SPIONs, because it highly influences the uptake in the different organs and the circulation time in the human body. The hydrodynamic diameter can be measured by photon correlation spectroscopy (PCS) or photon cross-correlation spectroscopy (PCCS) [8].

The Cotton-Mouton spectrometer (CMS) is an alternative method for measuring the hydrodynamic diameter of SPIONs [9]. The CMS uses the Cotton-Mouton effect (CME), which describes the effect that a magnetic field induces a birefringence in an anisotropic fluid. Thus, the CME describes the impact of an external magnetic field to the attenuation of a perpendicular light propagation of a laser beam.

2 Methods

The superparamagnetic ferrofluids used in the experiments presented here, are based on SPIONs dispersed in a liquid matrix. Generally, a SPION does not show any magnetization in equilibrium, but get magnetized as soon as it is subjected to a magnetic field. Additionally, the magnetic field induces birefringence in the anisotropic ferrofluid, an effect first described 1907 by Cotton and Mouton [10].

Linear polarized light is elliptically polarized due to a perpendicular magnetic field in a ferrofluid. This results in birefringence, and the difference in the optical pathway is determined by

$$\Delta n = n_o - n_e = C\lambda H^2, \quad (1)$$

where n_o and n_e are the refraction indices for the ordinary and extra-ordinary beam, λ is the wavelength of the light, H is the magnetic field strength, and C is the Cotton-Mouton constant [11].

The experimental setup is shown is Figure 1. A laser (λ = 635 nm) (1) is polarized by a polarizer (2) at an angle of 45° to the magnetic field. Afterwards, the beam passes through a coil arrangement (3) and is analyzed by a polarizer (4), and a quarter-wave plate (λ/4 plate) (5), which are positioned orthogonal to the polarizer (2). The beam intensity is measured by a photodiode (6).

A 3 ml cuvette (optical quartz glass) with a ferrofluid is placed inside the coil. A short rectangular current pulse generates a magnetic field inside the coil and the ferrofluid is magnetized correspondingly, i. e. the nanoparticles become structured in the magnetic field, and thus, birefringence is induced.

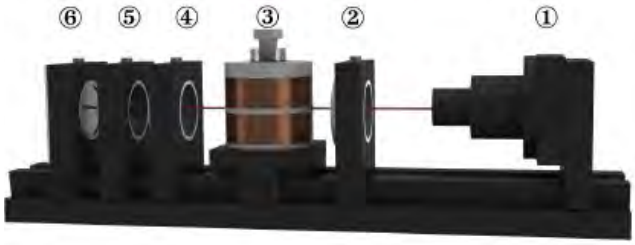

Figure 1: Experimental setup: (1) laser diode, (2), (4) polarizer, (3) coil and sample holder, (5) quarter wave plate (λ/4), (6) photodiode (Courtesy of Jan Krieger [9])

After switching off the magnetic field the magnetization of the ferrofluid relaxes due to Brownian motion and therefore the birefringence disappears. The resulting variation of light intensity of the laser beam can be measured with the photodiode. The recorded relaxation curve is fitted exponentially and used to estimate the Brownian relaxation time constant τ_B. This time constant, τ_B, is determined by

$$\tau_B = \frac{3\eta V_H}{k_B T}, \tag{2}$$

where η is the viscosity, k_B is the Boltzmann constant, V_H is the hydrodynamic volume and T is the temperature in Kelvin.

Magnetic field pulses used in this experiment are generated by a rectangular pulse of the current flowing through the coil. However, due to the time constant of the coil, the magnetic field does not fade instantaneously after switching off the current, and potentially covers Brownian relaxation, since the magnetic field still induces a magnetization of the ferrofluid. In order to avoid this effect and thus the distortion of the measurement of the relaxation time τ_B, the field cancellation must be accelerated accordingly.

The edge steepness of a magnetic pulse depends on the edge steepness of the current. The current propagation I for switching off the coil is given by

$$I = I_0 \cdot e^{-\frac{t}{\tau_c}}, \tag{3}$$

where I_0 is the initial current, t is the time and τ_c is the time constant of the exponential current propagation. τ_c is the sum of the time constant of the coil τ_l and the time constant τ_{switch}. The constant τ_{switch} describes the time needed to shut of the current. The overall relaxation time can then be described with

$$\tau_c = \tau_l + \tau_{switch} \quad \text{with} \tag{4}$$

$$\tau_l = \frac{L}{R} \tag{5}$$

and L as the inductivity and R as the resistor of the coil.

Figure 2 shows the first setup for the electric circuit of the coil current. The current pulse is generated by switching the source on and off. As the internal capacitance of the current source has a negative impact on the edge steepness the circuit is extended with a n-channel MOSFET. The circuit with the n-channel MOSFET driven by a signal generator is shown in Figure 3.

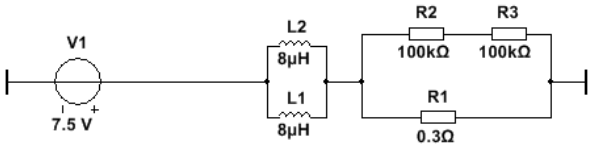

Figure 2: Coil circuit setup for the voltage switching circuit (V1 voltage source, L1 and L2 coil induction, R1-R3 resistors).

For both circuits the current time constant τ_c is estimated by measuring the proportional voltage at resistor R3. The recorded pulse edges are fitted to an exponential curve. The fit provides the time constant τ_c. The voltage is measured and recorded by an I/O-card (National Instruments, USA) and a PC.

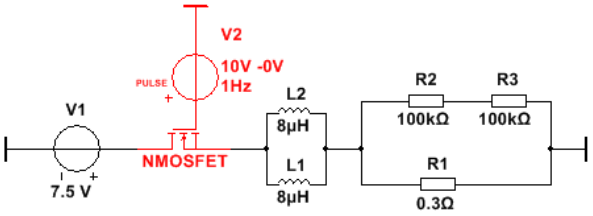

Figure 3: Coil circuit setup for the n-MOSFET switching circuit. The red parts are the parts that were added to the exiting circuit shown in Figure 2 (V1 voltage source, L1 and L2 coil induction, R1-R3 resistors, V2 pulse voltage source).

The radius r of the particle can be calculated by rearranging the formula for the Brownian relaxation (equation 2) and thus is given by

$$r_d = \left(\frac{\tau_B k_B T}{4\pi\eta}\right)^{\frac{1}{3}}. \tag{6}$$

3 Results

For each dataset 100 measurements are performed. Figure 4 shows the Brownian time constant τ_B in dependence of the time constant of current τ_c for switching of voltage source.

The mean τ_c is $1.1 \cdot 10^{-4}$ s with a standard deviation of $8.6 \cdot 10^{-6}$ s and the mean of τ_B is $2.6 \cdot 10^{-4}$ s with a standard deviation of $1.5 \cdot 10^{-5}$ s. The average of the par-

ticle radius is 44 nm with a standard deviation of $8.6 \cdot 10^{-10}$ s.
The distribution of the Brownian time constant τ_B in dependence of the time constant of current τ_c for the fast setup using the n-MOSFET is shown in Figure 5.

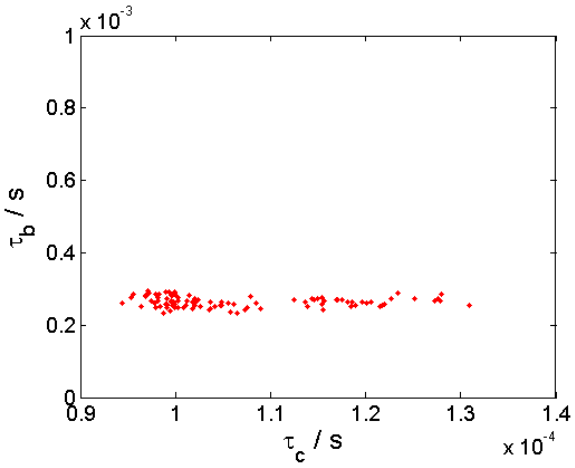

Figure 4: Distribution of the Brownian relaxation time constant τ_B in dependence of the time constant τ_c of the exponential current propagation for the voltage switching circuit.

The mean τ_c is $1.2 \cdot 10^{-5}$ s with a standard deviation of $2.6 \cdot 10^{-6}$ and the mean of τ_B is $3.5 \cdot 10^{-4}$ s with a standard deviation of $9.4 \cdot 10^{-5}$ s. The average of the particle radius is 47 nm with a standard deviation of $4 \cdot 10^{-9}$ s.

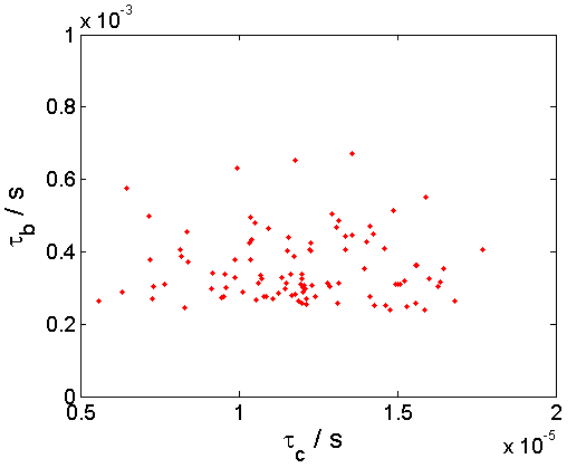

Figure 5: Distribution of the Brownian relaxation time constant τ_B in dependence of the time constant τ_c of the exponential current propagation for the n-MOSFET switching circuit.

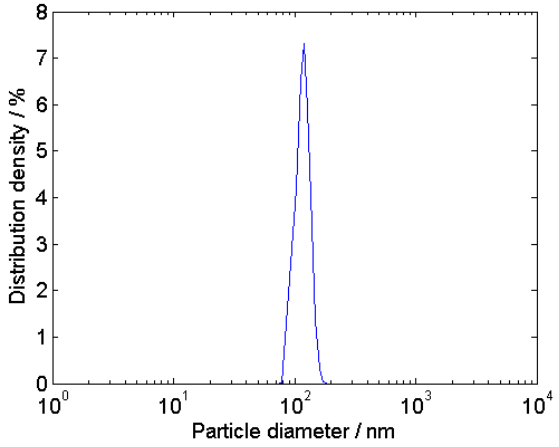

Figure 6: Distribution density of the particle diameter measured by PCCS.

As a reference method, photon cross-correlation spectrometry is used for the estimation of the hydrodynamic diameter of the particles in the used ferrofluid suspension. The measured ferrofluid solution is produced with nanoparticles of the same manufacture batch that was used for measurements with the CMS. The determined distribution density is shown in Figure 6. The maximum value of the distribution is at a diameter of 120 nm.

4 Discussion

The results in section 3 show that the setup with voltage source switching has a ten times higher τ_c than the setup with an n-MOSFET. For the adequate measurement of a particle radius of about 44 nm a τ_c of 10^{-4} s seem sufficient. This parameter range is achieved by the setup with the n-MOSFET. Thus, the measured τ_c indicates that the use of a n-MOSFET can reduce the switch-off times of the coil appropriately and enables an undisturbed measurement of the relaxation time τ_B.

Both setups show similar results for the measurement of the Brownian relaxation τ_B, which ranges from $2.6 \cdot 10^{-4}$ s to $3.5 \cdot 10^{-4}$ s. The large standard deviation of the time constant τ_B for n-MOSFET switching remains unclear at the present date and requires further investigation. In addition the measurement of light intensity is very susceptible to outer factors for example as a shift in the lighting conditions or vibrations.

Depending on similar relaxation times, the measurement of the particle radius shows results of 44 nm for the voltage source switching setup to 47 nm for the n-MOSFET switching setup. This corresponds to a particle diameter of 88 nm to 94 nm. The particle diameter estimated with the PCCS measurement is 120 nm. In comparison to the reference measurement using the PCCS this shows a deviation of about 30 nm.

As shown in Figure 6, the ferrofluid solution contains a distribution of different particle sizes. It is not yet clear, if the particles with different hydrodynamic diameters are associated with a corresponding variation of core diameters. PCCS and CMS are based on different physical properties of the particles, and therefore, differ in the results.

Actually, CME is – similar to MPI – based on the interaction between the magnetic field and the nanoparticles in a liquid matrix. Hence, the capability of structuring the fluidal matrix by the magnetic field is associated with the particle core-size and not with the hydrodynamic diameter. However, the incongruity of the presented results needs further investigations.

5 Conclusion

Krieger et al. already demonstrated that the determination of the hydrodynamic diameter of SPIONs is possible using the Cotton-Mouton effect. This contribution introduces the improvement of the coil circuit from a voltage-supply switching setup to an n-MOSFET switching setup. This leads to an accelerated field cancelling, which recovers the time constant of the Brownian relaxation.

Further investigation of the challenges mentioned in section 4 has to be carried out, but first experimental results show that the use of the Cotton-Mouton effect for the measurement of the hydrodynamic diameter is a promising alternative technique to PCCS measurements.

Acknowledgements

The reseach on magnetic nanoparticle analytics at the Institute of Medical Engineering is funded by the European Union Seventh Framework Programme (FP7/2007-2013) under grant agreement n° 604448.

References

[1] Gutrath, B. S.; Beckmann, M.; Buchkremer A.; Eckert, T.; Timper, J.; Leifert, A.; Richtering, W.; Schmitz, G.; Simon, U.: Size-dependent multispectral photoacoustic response of solid and hollow gold nanoparticles, Nanotechnology 23, pp. 225707-1-10, 2012, doi: 10.1088/0957-4484/23/22/225707.

[2] Hyafil, F.; Cornily, J.-C., Feig, J. E., Gordon, R.; Vucic, E.; Amirbekian, V.; Fisher, E. A.; Fuster, V.; Feldman, L. J.; Fayad, Z. A.: Noninvasive detection of macrophages using a nanoparticulate contrast agent for computed tomography, Nature Medicine 13, pp. 636-641, 2007, doi: 10.1038/nm1571

[3] Reimer, P.; Balzer, T.: Ferucarbotan (Resovist): a new clinically approved RES-specific contrast agent for for contrast-enhanced MRI of the liver:properties, clinical development, and applications, European Radiology 13(6), pp. 1266-1276, 2003, doi: 10.1007/s00330-002-1721-7

[4] Gleich, B.; Weichenecker, J.: Tomographic imaging using nonlinear response of magnetic particles, Nature 435(30), pp. 1214, 2005, doi:10.1038/nature03808.

[5] Goya, G.; Lima, E. Jr.; Arelaro, A. D.; Torres, T.; Rechenberg, H. R.; Rossi, L.; Marquina, C.; Ibarra, M. R.: Magnetic hyperthermia with Fe_3O_4 nanoparticles: the influence of particle size on energy absorption, IEEE Transactions on Magnetics 44(11), pp. 4444-4447, 2008, doi: 10.1109/TMAG.2008.2003508.

[6] Ferguson, R. M.; Minard, K. R.; Krishnan, K. M.: Optimization of nanoparticle core size for magnetic particle imaging, Journal of Magnetism and Magnetic Materials 321(10), pp. 1548–1551, 2009, doi:10.1016/j.jmmm.2009.02.083.

[7] Weizenecker, J.; Borgert, J.; Gleich, B: A simulation study on the resolution and sensitivity of magnetic particle imaging, Phys. Med. Biol. 52, pp 6363–6374, 2007, doi:10.1088/0031-9155/52/21/001.

[8] Witt, W.; Aberle, L.; Geers, H.: Measurement of particle size and stability of nanoparticles in opaque suspensions and emulsions with photon cross correlation spectroscopy, Particulate Systems Analysis, Harrogate, 2003.

[9] Krieger, J.; Köhler, K.; Gräser, M.; Lüdtke-Buzug, K.: Construction of a spectrometer to measure the Cotton-Mouton effect of superparamagnetic iron oxide nanoparticles, Biomed. Tech. 58, Suppl. 1, 2013, doi 10.1515/bmt-2013-4102.

[10] Cotton, A.; Mouton, H., Nouvelle propriete optique (birefringence magnetique) de certains liquids organiques non colloïdaux, Comptes Rendus hebdomadaires des Seances de l'Academie des Sciences Paris, 145, 1907.

[11] Groß, C.; Romanus, E.; Glöckl, G.; Weber, P.; Weitschies, W.: Magneto-Optical Relaxation of Ferrofluids, European Cells and Materials 3(2), pp.22, 2002.